Atmos. Chem. Phys. Discuss., 14, 541–591, 2014
www.atmos-chem-phys-discuss.net/14/541/2014/
doi:10.5194/acpd-14-541-2014
© Author(s) 2014. CC Attribution 3.0 License.

Atmospheric Chemistry and Physics Discussions

This discussion paper is/has been under review for the journal Atmospheric Chemistry and Physics (ACP). Please refer to the corresponding final paper in ACP if available.

Impact of black carbon aerosol over Italian basin valleys: high resolution measurements along vertical profiles, radiative forcing and heating rate

L. Ferrero[1], M. Castelli[2], B. S. Ferrini[1], M. Moscatelli[1], M. G. Perrone[1], G. Sangiorgi[1], G. Rovelli[1], L. D'Angelo[1], B. Moroni[3,6], F. Scardazza[3], G. Mocnik[4], E. Bolzacchini[1], M. Petitta[3], and D. Cappelletti[5,6]

[1]POLARIS Research Centre, Department of Earth and Environmental Sciences, University of Milano-Bicocca, Piazza della Scienza 1, 20126, Milan, Italy
[2]EURAC Institute for Applied Remote Sensing, Viale Druso 1, 39100, Bolzano, Italy
[3]DICA, Università degli Studi di Perugia, Via G. Duranti 93, 06125 Perugia, Italy
[4]Aerosol d.o.o., Kamniska 41, 1000 Ljubljana, Slovenia
[5]Dipartimento di Chimica, Biologia e Biotecnologie, Università degli Studi di Perugia, via elce di Sotto 8, 06123 Perugia, Italy
[6]SMAArt, Università degli Studi di Perugia, Pza. dell'Università 1, 06100 Perugia, Italy

Received: 4 December 2013 – Accepted: 13 December 2013 – Published: 9 January 2014

Correspondence to: L. Ferrero (luca.ferrero@unimib.it)

Published by Copernicus Publications on behalf of the European Geosciences Union.

ACPD
14, 541–591, 2014

Abstract

This study presents the first measured high resolution vertical profiles of black carbon and calculation of aerosol radiative forcing and atmospheric heating rates in the lower troposphere, over Italy and Europe. The calculation is based on vertical profiles of black carbon, aerosol number size distribution and chemical composition measured over three Italian basin valleys (Po Valley, Terni Valley and Passiria Valley) by means of a tethered balloon equipped with a micro-Aethalometer, an optical particle counter (OPC), a cascade impactor and a meteorological station. Experimental measurements allowed first the calculation of the aerosol optical properties. In this respect, the aerosol refractive index was calculated along height using the effective medium approximation applied to aerosol chemical composition; Mie calculations were performed on the base of the OPC number-size distribution which was corrected for the ambient aerosol refractive index. The obtained vertical profiles of aerosol optical properties were validated with AERONET data and were used as input to the radiative transfer model libRadtran. Vertical profiles of direct aerosol radiative forcing, atmospheric absorption and heating rate were calculated.

Reported results evidenced common behaviours along height over the investigated basin valleys (an orographic feature present elsewhere in Europe): at the mixing height a marked a concentration drop of both BC (range: -48.4 ± 5.3 % to -69.1 ± 5.5 %) and particle number concentration (range: -23.9 ± 4.3 % to -46.5 ± 7.3 %) was evidenced. More in details, the percentage decrease of BC along height was higher than that measured for aerosol and thus, the BC content of the aerosol decreased along height; correspondingly the Single Scattering Albedo increased along height (range: $+4.9 \pm 2.2$ % to $+7.4 \pm 1.0$ %). Therefore, the highest atmospheric absorption was observed below the mixing height (range: $+0.5 \pm 0.1\,\mathrm{W\,m^{-2}}$ to $+2.5 \pm 0.2\,\mathrm{W\,m^{-2}}$) with the associated heating rate characterized by a vertical negative gradient (range: $-0.5\,\mathrm{K\,day^{-1}\,km^{-1}}$ to $-6.8\,\mathrm{K\,day^{-1}\,km^{-1}}$). As a result, the Black Carbon loaded below the mixing height

ACPD
14, 541–591, 2014

potentially weakens the ground-based thermal inversions (common over basin valleys) thus promoting an increase of the atmospheric dispersal conditions.

1 Introduction

Atmospheric aerosols influence the Earth's climate trough different effects: direct effects (sunlight absorption and scattering), indirect effects (i.e. modifying the lifetime of the clouds) and semi-direct effects (i.e. affecting the atmospheric thermal structure) (Ramanathan and Feng, 2009; Koren et al., 2008; IPCC, 2007; Koren et al., 2004; Kaufman et al., 2002). The instantaneous direct radiative effect (DRE) due to the aerosol load can reach values as high as $\sim -50\,W\,m^{-2}$ and ~ -10–$20\,W\,m^{-2}$ at the surface and at the Top of Atmosphere (TOA), respectively (Perrone and Bergamo, 2011).

Among the whole aerosol constituents, Black Carbon (BC) plays a crucial role as it is reported to be the second most important anthropogenic climate forcing agent (Ramanathan and Carmichael, 2008; Bond et al., 2013). The averaged BC-DRE at the TOA was estimated by many authors ranging between $+0.08\,W\,m^{-2}$ and $+1.4\,W\,m^{-2}$ (Samset et al., 2013; Ramanathan and Carmichael, 2008; Jacobson, 2001) with a best estimate of $+0.71\,W\,m^{-2}$ (Bond, 2013).

Moreover, besides the global effect at the TOA and, unlike CO_2, BC affects the climate by both warming the atmosphere ($\sim +2.6\,W\,m^{-2}$ and in some cases up to $\sim +75\,W\,m^{-2}$) and, at the same time, cooling ("masking") the surface ($\sim -1.7\,W\,m^{-2}$ and in some cases up to $\sim -60\,W\,m^{-2}$) (Chakrabarty et al., 2012; Ramanathan and Carmichael, 2008).

The wide range of reported BC-DRE values is due to different reasons: the whole complexity of aerosol chemistry (i.e. mixing state) (Ramana et al., 2010), the surface albedo (Seinfeld and Pandis, 1998) and most important, the spatial heterogeneity in terms of concentrations (horizontal and vertical) due to its low lifetime (measured in weeks) compared to CO_2 (Samset et al., 2013; Cape et al., 2012). Recent modeling of the BC-DRE (Samset et al., 2013; Zarzycki and Bond, 2010) evidenced opposing

ACPD
14, 541–591, 2014

behaviours, with a DRE effect mainly located in the lower or in the upper troposphere depending on the BC location along the profile. The resulting overall degree of uncertainty attributable to the assumptions about the vertical distribution of BC was estimated to be in the range 20–50 %.

Indeed, the vertical heterogeneity of BC and its DRE influences the atmospheric thermal structure with heating rates differentiated along height within a range of ∼ 0.5–2 K day^{-1} (Chakrabarty et al., 2012; Ramana et al., 2010; Tripathi et al., 2007); as a results different kinds of feedback can take place, such as those on clouds dynamics (Bond, 2013), on regional circulation systems (i.e. monsoons) and on the Planetary Boundary Layer (PBL) dynamics (Ramanathan and Feng, 2009; Ramanathan and Carmichael, 2008).

Since it is likely that different regions have different sensitivity to all of these processes (Bond, 2013) and also that modeling of and observational constraints on the BC vertical distribution are particularly poor, there is the need to measure the BC vertical distribution on a regional scale: from areas characterized by anthropogenic emissions and atmospheric stability conditions to areas characterized by long-range transport phenomena (Samset et al., 2013; Corrigan et al., 2008; Ramana et al., 2007).

However, up till now, BC profiles were globally scarce compared with ground-level data, even if recently many vertical profiles have been reported for the Asian Region (Safai et al., 2012; Babu et al., 2011; Ramana et al., 2010; Corrigan et al., 2008; Tripathi et al., 2007) and some over the ocean (Schwarz, 2013, 2010). Conversely, a deficiency of BC profiles exists especially over Europe, where reported campaigns were limited in time and/or in space (McMeeking et al., 2010; Schwarz et al., 2006). One reason of this lack may lie in the cost of such measurements, especially when conducted using aircrafts, even if, other direct methods (tethered balloons, UAVs) could be used to collect long-term measurements at a reasonable cost (Ferrero et al., 2012; Corrigan et al., 2008; Maletto et al., 2003). Moreover, measurements conducted with airplanes cannot provide high resolution data in the first hundreds meters above the surface,

ACPD
14, 541–591, 2014

where most of the emissions take place and do not usually allow capturing aerosol dynamics within and across the mixing layer.

In this respect, there is a clear need to improve the knowledge about aerosol vertical profiles over Europe where a plethora of different territories and situations are present. This is true especially over Italy. The complex orography of Italy represents an interesting and significant case study for black carbon and aerosols monitoring in complex-orography regions. The Italian territory results in a multitude of basin valleys of various sizes, in which urban and industrial centers usually lie. These valleys represent important areas where low wind speeds and conditions of atmospheric stability are common, thus promoting the formation of strong vertical aerosol (and BC) gradients in the lower troposphere (Moroni et al., 2013, 2012; Ferrero et al., 2011a; Carbone et al., 2010; Rodriguez et al., 2007). In Italy the only measured vertical profiles of BC and absorption coefficient are reported for a short campaign in Ferrero et al. (2011a).

Hence, this paper tries to fill a relevant gap in atmospheric science reporting, for the first time in Italy and Europe, a comparative study of BC and aerosol vertical profiles measured over three different basin valleys (Po Valley, in Northern Italy; Terni Valley in the Central Apennines; and Passiria-Val Venosta Valleys in the Alps) from which an introductory indication of the possible feedback induced by BC concentration in the lower troposphere, calculating high resolution DRE and heating rates profiles. The aforementioned behaviours were investigated in relationship to mixing height (MH) dynamics.

In the next sections we briefly describe the sampling sites (Sect. 2.1) and the vertical profile measurements (Sect. 2.2). BC and aerosol chemistry determination are illustrated in Sects. 2.2.1 and 2.2.2. The OPC size-distribution correction and the optical properties calculation using the Mie theory are described in Sect. 2.3 and the radiative transfer in Sect. 2.4. Results and discussion will follow in Sect. 3 with conclusions in the final Sect. 4.

ACPD
14, 541–591, 2014

2 Experimental

2.1 Sampling sites

Balloon soundings were carried out during winter 2010 over three basin Valleys in the following sites (Fig. 1a):

1. Terni (TR, 42°33′58″ N, 12°38′56″ E, 122 m a.s.l.), located in the Terni Valley in Central Italy. The Terni Valley (~ 50 km^2) is surrounded by mountains on three sides (NNE, SE and SW) and hosts the medium-sized town of Terni, with the largest stainless-steel production site in Europe and various other industries. In wintertime, wind speed is low and the aerosol dispersion is limited with height. A full description of the site concerning the aerosol properties (chemistry, sources and vertical profiles) is reported in Moroni et al. (2013, 2012) and Ferrero et al. (2012). Within the present work, vertical aerosol and BC profiles were measured over Terni from 27 January to 4 February for a total of 40 profiles.

2. Milan (MI, 45°31′19″ N, 9°12′46″ E, 136 m a.s.l.), which is located in the Po Valley (~ 46 000 km^2, Northern Italy) in the midst of an extensive conurbation that is the most industrialized and heavily populated area in the Po Valley. In the Po Valley stagnant conditions often occur causing a marked seasonally variation of PM concentrations within the mixing layer. Balloon soundings were conducted at the Torre Sarca sampling site within the Milano-Bicocca University Campus (north Milano, active from 2005 for aerosol characterization both at ground-level and along vertical profiles) in the northern side of Milan. A full description of the site and the related aerosol properties (vertical profiles, chemistry, sources, and toxicity) are reported in Ferrero et al. (2010), in Perrone et al. (2013) and in Sangiorgi et al. (2011). Within the framework of the 2010 winter campaign, vertical aerosol and BC profiles were measured over Milan from 12 February to 25 February for a total of 36 profiles.

ACPD
14, 541–591, 2014

3. Merano (ME, 46°38′52″ N, 11°10′13″ E, 272 m a.s.l.), which is located at the intersection of two main Alpine Valleys: Val Venosta (E–W orientation) and Val Passiria (N–S orientation) allowing the air masses to be transported both from Continental Europe (North) and from the Po Valley (South). The sampling site was located in a rural area at the location of the local authority background station for air quality monitoring of the local authorities ("Merano 2 station", APPA). A full description of the site and pollution in the surrounding valleys are reported in Emili et al. (2010, 2011). Within the 2010 winter campaign, vertical aerosol and BC profiles were measured over Merano from 3 March to 13 March for a total of 40 profiles.

2.2 Vertical profile measurements

BC and aerosol profile measurements were carried out over TR, MI and ME by means of a helium-filled tethered balloon (diameter 4.5 m, volume 47.8 m^3, payload 40 kg, Fig. 1b) equipped with an instrumental package consisting of: (1) the micro-Aethalometer microAeth® AE51 (Magee Scientific) to measure the BC concentrations and the absorption coefficient at 880 nm; (2) an optical particle counter (OPC, 1.107 *"Environcheck"* Grimm, 31 class-sizes ranging from 0.25 µm to 32 µm) for the particle number size distribution determination; (3) a portable cascade impactor (Sioutas with Leland Legacy pump, SKC) to collect $PM_{2.5}$ samples at different heights (Sect. 2.2.2); (4) a meteorological station (LSI-Lastem: pressure, temperature and relative humidity).

An electric winch controlled the balloon ascent/descent rate which was set at 30.0 ± 0.1 m min^{-1}; a measurement time resolution of 6 s was chosen for each instrument, giving 3.0 m of measurement vertical resolution. The maximum height reached during each flight depended on atmospheric conditions and the location; for the majority of profiles, the maximum height was between 600 and 800 m a.g.l.

Vertical aerosol profiles allowed the determination of the mixing height (MH) by means of a gradient method, as the aerosol act as tracer of atmospheric plumes integrating the effects of turbulent forces (thermal and mechanical) along height; the

ACPD
14, 541–591, 2014

gradient method's ability to infer the MH has yet been assessed in previous works (Ferrero et al., 2011a, b and 2010). The MH will be used to calculate averaged aerosol and BC profiles for each site (Sect. 3.2)

2.2.1 Aethalometer data: Black Carbon and the related absorption coefficient

BC and absorption coefficient profiles were determined using the microAeth® AE51 (250 g, 117 mm × 66 mm × 38 mm). The AE51 measures the light attenuation (ATN) at 880 nm induced by BC through a PTFE-coated borosilicate glass fiber filter (Fiberfilm™ Filters, Pall Corporation) continuously loaded by the aerosols during sampling. ATN is calculated as:

$$\mathrm{ATN} = 100 \cdot \ln(I_0/I) \tag{1}$$

where I_0 and I are the light intensities transmitted throughout a reference blank spot and the aerosol-laden 3 mm diameter sample spot of the filter.

The attenuation coefficient of the filtered aerosol particles, b_{ATN}, can be derived from ATN as follows Weingartner et al. (2003):

$$b_{\mathrm{ATN}} = \frac{A}{100Q}\frac{\Delta \mathrm{ATN}}{\Delta t} \tag{2}$$

where ΔATN indicates the ATN variation during the time period Δt, A is the sample spot area ($7.1 \times 10^{-6}\,\mathrm{m}^2$) and Q is the volumetric flow rate ($2.5 \times 10^{-6}\,\mathrm{m}^3\,\mathrm{s}^{-1}$). The aerosol absorption coefficient, b_{abs}, is calculated as follows:

$$b_{\mathrm{abs}} = \frac{b_{\mathrm{ATN}}}{C \cdot R(ATN)} \tag{3}$$

where C and R(ATN) are the multiple scattering optical enhancement factor and the aerosol loading factor, respectively. Briefly, the constant optical enhancement factor C

ACPD
14, 541–591, 2014

compensates for the enhanced optical path through the filter caused by multiple scattering induced by the filter fibres themselves (Schmid et al., 2006; Arnott et al., 2005, Weingartner et al., 2003). For the AE51 microAeth® C is 2.05 ± 0.03 (at $\lambda = 880$ nm) (Ferrero et al., 2011). Conversely, R(ATN) compensates for the nonlinearity – the loading effect due to an increase in the aerosol absorption over time, which in turn results in a reduction in the optical path; it is needed only when ATN becomes higher than 20 (Schmid et al., 2006; Arnott et al., 2005; Weingartner et al., 2003). In this study, the experimental design allows to neglect the use of R(ATN): all BC vertical profiles were conducted by changing the filter ticket between profiles, thus resulting in ATN always lower than 20 as recommended by Weingartner et al. (2003). It is necessary to underline that, to rightly estimate DRE profiles, multiple-wavelenghts optical properties are needed (Sect. 2.4); thus the b_{abs} derived from the micro-Aeth® AE51 at 880 nm was used in this study during the validation of the optical properties calculation (Sects. 2.3 and 3.2.2) to verify the correct shaping of them in order to avoid the presence of compensatory effects along profiles.

Finally, to determine the BC ambient concentration the apparent mass attenuation cross-section ($\sigma_{ATN} = 12.5\,m^2\,g^{-1}$) is needed; it is defined for the BC collected on the PTFE-coated borosilicate glass fiber filter (considering the optical components of the instrument) and is provided by the manufacturer. The BC concentrations are determined as follows:

$$BC = \frac{b_{ATN}}{\sigma_{ATN}} \quad (4)$$

2.2.2 Aerosol chemistry determination

The knowledge of aerosol chemical composition along height is fundamental to calculate the aerosol refractive index along vertical profiles (Sect. 2.3.1), which is the basis for the correction of the OPC size-distribution (Sect. 2.3.2), for the determination of aerosol optical properties and DRE calculations (Sects. 2.3, 2.4, 3.2 and 3.3).

ACPD
14, 541–591, 2014

BC concentrations were measured with a micro-Aethalometer, as reported in the previous section (2.2.1). Moreover, at ME site only, a 7-λ Aethalometer (AE31, Magee Scientific) was also present at ground level, and recorded ground BC concentrations continuously during the campaign.

In order to complete the aerosol chemistry along profiles, $PM_{2.5}$ samples were collected during balloon flights at two different heights: ground-level (below the mixing height: BMH), and above the mixing height (AMH: ~ 600 m a.g.l., depending on the atmospheric conditions and the location).

$PM_{2.5}$ at ground level was sampled using the TECORA ECHO-PM gravimetric system ($PM_{2.5}$ sampling head, flow 2.3 $m^3 h^{-1}$; STERLITECH Polycarbonate filters, $\varnothing = 47$ mm), while at higher altitudes it was sampled using a balloon-borne portable cascade impactor (Sioutas type with Leland Legacy pump, SKC; 9 L min^{-1}; STERLITECH Polycarbonate filters, $\varnothing = 37$ mm).

$PM_{2.5}$ samples were analyzed to determine the water-soluble ionic fraction (Perrone et al., 2012). Water-soluble ions were extracted by ultrapure water (Milli-Q) in an ultrasonic bath (20 min; SOLTEC SONICA®). Cations (Na^+, NH_4^+, K^+, Mg^{2+} and Ca^{2+}) were determined by a Dionex ICS-90 (Ion Pac CS12A-5 µm column, using methansulfonic acid as eluent in an isocratic concentration of 0.4 M at 0.5 mL min^{-1}). Anions (Cl^-, NO_3^-, SO_4^{2-}), together with mono and dicarboxylic acids (formiate, acetate, propionate, oxalate, malonate, succinate, glutarate), were analysed by a Dionex ICS-2000 (Ion Pac AS11A-5 µm column using KOH at 1.2 mL min^{-1} with a gradient elution between 1.0 mM and 28 mM).

The organic matter (OM) fraction was estimated from PM data (Sect. 2.2.1) both BMH and AMH considering the OM fraction derived from wintertime averaged data contained in previous works (Perrone et al., 2012; Ferrero et al., 2011a). Moreover, for the purpose of the refractive index estimation the OM was divided into: the water-soluble OM (WSOM) and the water-insoluble OM (WINSOM). They were calculated using a WSOM/TC (TC = total carbon) coefficient of 0.33 for BMH data and of 0.61 for AMH data during wintertime as derived from data reported in Carbone et al. (2010).

ACPD
14, 541–591, 2014

Finally, because the determination of aerosol DRE requires the knowledge of the aerosol properties along the whole atmospheric column, the intrinsic limit due to the maximum height of balloon flights (800 m a.g.l.) was overcome using a standard continental-average profile of aerosol chemistry, as defined by the OPAC model (Hess, 1998), for aerosol over 1 km.

The reliability of all the aforementioned assumptions will be discussed in Sect. 3.2.2 through a careful validation of the results with AERONET (columnar validation) and Aethalometer data (validation along the profile).

2.3 Aerosol optical properties

Aerosol optical properties were calculated along vertical profiles using a Mie code (Bohren and Huffman, 1983) to subsequently evaluate the aerosol DRE (Sects. 2.4 and 3.3). For this purpose five wavelengths (270, 441, 675, 880 and 3200 nm) were considered in order to cover the solar spectrum (Sect. 2.4); three of them (441, 675 and 880 nm) represent the main bands used in the AERONET network allowing the validation of the methodology presented here using AERONET data.

The optical properties needed as input for the DRE profiles calculation (Sect. 2.4) are the extinction coefficient b_{ext} (the sum of scattering and absorption coefficients), the single scattering albedo (SSA) and the aerosol phase function (P).

The scattering and absorption coefficients (b_{sca} and b_{abs}) were calculated from the integration of the corresponding scattering and absorption efficiencies (Q_{sca} and Q_{abs}) over the whole number-size distribution (Seinfeld and Pandis, 1998):

$$b_{sca/abs} = \int_0^{D_p^{max}} \frac{\pi D_p^2}{4}(m,x)n(D_p)\mathrm{d}D_p \quad (5)$$

where m and x are the aerosol complex refractive index and the size parameter, respectively while, $n(D_p)$ represents the number-size distribution as a function of aerosol diameter (D_p).

ACPD
14, 541–591, 2014

From the knowledge of b_{sca} and b_{abs} profiles, the SSA along height was calculated:

$$SSA = \frac{b_{sca}}{b_{sca} + b_{abs}} \quad (6)$$

Finally, the aerosol phase function P is defined as the normalization of the Mie scattering function over the whole 4π spherical angle. For an aerosol characterized by a complex refractive index m and a size parameter x, $P(\theta, x, m)$ is defined as follows (Crosbie and Davidson, 1985):

$$P(\theta, x, m) = \frac{i(\theta, x, m)}{\frac{1}{2}\int_0^{\pi} i(\theta, x, m) \sin\theta \mathrm{d}\theta} \quad (7)$$

where $i(\theta)$ is the Mie scattering function which, for unpolarized light, is the average between the perpendicular and parallel components: $i_1(\theta)$ and $i_2(\theta)$ respectively.

Equations (5)–(7) require an accurate knowledge of the aerosol refractive index and size-distribution. In the following sections we report the methodology followed to calculate the aerosol refractive index from the measured aerosol chemical composition (Sect. 2.3.1) and the aerosol size distribution from OPC data (Sect. 2.3.2).

2.3.1 Aerosol refractive index

The complex refractive index ($m = n + ik$) of aerosol was calculated considering a hybrid internal/external mixing scenario. The coarse ($D_p > 1$ µm) and fine ($D_p \leq 1$ µm) particles were considered externally mixed, each one characterized by its proper value of m (Ferrero et al., 2011a). Coarse particles ($D_p > 1$ µm) were assumed to be composed of dust, while m for fine particles was calculated from the measured $PM_{2.5}$ chemical composition (Sects. 2.2.2 and 3.1) using the Bruggeman mixing rule (Stier et al., 2007; Aspnes, 1982; Heller, 1965; Bruggeman, 1935):

$$\sum_{i=1}^{n} f_i \frac{\varepsilon_i - \varepsilon_{eff}}{\varepsilon_i + 2\varepsilon_{eff}} = 0 \quad (8)$$

ACPD
14, 541–591, 2014

where ε_{eff} is the complex effective dielectric constant of the mixture ($m \approx \sqrt{\varepsilon_{\text{eff}}}$) and ε_i and f_i are the complex dielectric constant, and the volume fraction, of the ith component respectively. This approach is also known as "effective medium approximation" (EMA) as inclusions (aerosol components) are considered embedded in the effective medium itself. The Bruggeman mixing rule simulates the real complexity of aerosols considering all possible positions of each component (BC, water soluble materials, organics...) in an aerosol particle avoiding the dilemma of the choice of a host medium among the various aerosol components; this choice, instead, has to be made when using other mixing rules, such as the Maxwell–Garnett and the Lorentz–Lorenz (Liu and Daum, 2008; Stier et al., 2007; Aspnes, 1982; Heller, 1965). Moreover, the Bruggeman mixing rule avoids the risk of overestimating the imaginary part (k) of m, as instead happens using both the linear volume-average and the linear mass-average mixing rules in the presence of highly absorbing inclusions (i.e. BC) in a non-absorbing medium (i.e. NH_4NO_3 and $(NH_4)_2SO_4$) (Stier et al., 2007; Lesins et al., 2002; Chýlek et al., 1995).

Vertical profiles of aerosol refractive index were calculated from the aerosol chemical composition along height using EMA; in this respect the missing mass was assigned equally to both water and dust (Ferrero et al., 2011a) since it has been shown that a certain amount of water is bound to particles (Subramanian et al., 2007; Hueglin et al., 2005; Rees et al., 2004), and also that this amount is comparable to dust in winter (Hueglin et al., 2005; Rees et al., 2004). Densities (ρ) of pure compounds were used to estimate the volume fraction of each aerosol component (Fierz-Schmidhauser et al., 2010; Pesava et al., 2001; Chazette and Liousse, 2001; Heller, 1965).

A detailed description of refractive indexes and densities of pure aerosol components used in the calculation, and yet successfully applied along vertical profiles, is reported in Ferrero et al. (2011a); here we briefly summarize these choices. Refractive indexes as a function of λ for water-soluble components, water-insoluble components and dust were that reported by Hess (1998) while, the chosen value for the BC refractive index was that suggested in Bond and Bergstrom (2006): $1.85 + i0.71$. However, the latter value is referred to 550 nm only and thus, the wavelength dependence of BC

ACPD
14, 541–591, 2014

refractive index reported in Ackerman and Toon (1982), and yet successfully used in Ferrero et al. (2011a), was applied to the Bond and Bergstrom (2006) value in order to calculate the aerosol optical properties over the whole solar spectrum. The density (ρ) values were: 1.75, 1.45, 1.45 and 2.6 g cm^{-3} for ionic components, WSOM, WINSOM and dust, respectively; they lie at the mid-point of published data reported in Ferrero et al. (2011a) and references therein.

Finally, the aerosol refractive index was determined point by point along vertical profiles, considering the hygroscopic growth of the aerosol:

$$D_{pw} = D_p \cdot \left(\frac{1 - RH}{1 - DRH} \right)^{-\varepsilon} \quad (9)$$

where RH is ambient relative humidity, D_p is the aerosol diameter at the Deliquescence Relative Humidity (DRH) and D_{pw} the aerosol diameter at ambient RH; ε is the coefficient controlling the aerosol's hygroscopic growth. Since the ground-level chemical composition of dry aerosol measured in TR, MI and ME (Sect. 3.1.2) is similar to that reported in Randriamiarisoa et al. (2006) and Raut and Chazette (2008), we set ε accordingly to 0.26.

DRH was estimated for each site, along the profiles, from the aerosol's chemical composition using the thermodynamic Aerosol Inorganic Model (E-AIM Model-II) (Clegg et al., 1998) (http://www.aim.env.uea.ac.uk/aim/aim.php). This is a state-of-the-art aerosol thermodynamic model for the H^+-NH_4^+-SO_4^{2-}-NO_3^--carboxylic acids-H_2O composition of the aerosol (Zhang et al., 2000). This model was yet successfully used to accurately predict aerosol DRH (Ferrero et al., 2013a, b; Hueglin et al., 2005; Pathak, 2004). Calculated DRHs are discussed in Sect. 3.1.2. From hygroscopic growth, the EMA was applied point by point along height to calculate the final aerosol refractive index every 3.0 m for each profile.

As the aforementioned choices (EMA mixing rule, m and ρ for pure components, hygroscopic growth) can seriously affect the optical properties calculation, the calculated aerosol optical properties were subjected to a detailed validation procedure based on

ACPD
14, 541–591, 2014

the comparison of different parameters (i.e. refractive index, SSA, AOD...) with those independently obtained by the Aerosol Robotic Network (AERONET) (Sect. 3.2.1).

2.3.2 Aerosol size distribution

The determination of aerosol optical properties requires an accurate aerosol size-distribution estimation. In this study, the aerosol size-distribution was measured using the OPC Grimm 1.107 (λ = 655 nm). Two effects affect the aerosol size-distribution measured by OPCs: the "undersizing" and the "truncation effect". They need to be compensated to calculate the optical properties.

"Undersizing" occurs due to the OPC calibration with polystyrene latex spheres (PLS, m = 1.58 at 655 nm; Ma et al., 2003) whose refractive index has usually a larger real part compared to ambient aerosol (Sect. 3.2.1) (Guyon et al., 2003; Liu and Daum, 2008; Schumann, 1990). Thus, the OPC size channels were corrected to account for the ambient aerosol refractive index m; the OPC response function (S: the partial light scattering cross section of the particle related to the specific optical design of the OPC) was computed at 655 nm as follows (Baron and Willeke, 2005; Heyder and Gebhart, 1979):

$$S(\theta_0, \Delta\Omega, x, m) = \frac{\lambda^2}{4\pi^2} \iint_{\Delta\Omega} i(\theta, \phi, x, m) \sin\theta \mathrm{d}\theta \mathrm{d}\phi \quad (10)$$

where θ_0 represents the mean scattering angle of the optical arrangement, $\Delta\Omega$ the receiver aperture, x the dimensionless size parameter, m the refractive index and $i(\theta, \varphi, x, m)$ the Mie scattering function composed by the perpendicular and parallel components: $i_1(\theta, x, m)$ and $i_2(\theta, x, m)$ respectively. The optical arrangement of the OPC 1.107 consists of: (1) a wide angle parabolic mirror (121°, from 29.5° to 150.5°, θ_0 = 90°) that focuses scattered light on the photodetector located on the opposite side; (2) 18° of direct collected scattered light on the photodetector (from 81° to 99°, θ_0 = 90°) (Heim et al., 2008).

ACPD
14, 541–591, 2014

The response function was calculated both for PLS (S_{PLS}) and for ambient aerosol (S_{AMB}) along each vertical profile, within and above the mixing layer. The refractive indexes of ambient aerosol used in S_{AMB} calculations were calculated as reported in Sect. 2.3.1: (1) m for fine particles calculated applying the EMA (Sect. 2.3.1) and (2) dust refractive index for coarse particles. Table 1 shows the columnar means of the new size corrected channels for TR, MI and ME: results agree with literature studies (Ferrero et al., 2011a; Liu and Daum, 2008; Schumann, 1990).

The second effect, which must be taken into account before calculating optical properties of aerosol, is the "truncation effect": the accumulation mode is only partially measured (lowest equivalent PLS size of OPC: 0.25 µm) and no measurements are available for Aitken mode particles (D_p < 0.1 µm). Conversely, the coarse mode results completely defined. A negligible error (~ 2–4 %) comes from not considering the Aitken mode in the optical properties calculation (Bond and Bergstrom, 2006; Guyon et al., 2003; Liu and Daum, 2008; Randriamiarisoa et al., 2006); however, the "truncation effect" in the accumulation mode cannot be neglected.

Thus, a log-normal interpolation of the aerosol number-size distribution was conducted for each OPC data measured along vertical profiles to complete the aerosol size distribution function $n(D_p)$. This procedure has already been successfully used by Ferrero et al. (2011a), Deshler et al. (2003) and Angelini et al. (2009). This procedure makes the calculated optical properties closely dependent on the reliability of the number-size distribution interpolation, hence its accuracy is discussed in Sect. 3.2.1.

2.4 Radiative transfer code

Aerosol scattering and absorption of solar radiation modify the intensity and spectral distribution of surface incoming solar radiation. These effects, which are called here the direct radiative effect (DRE), can be quantified as the difference between the atmospheric conditions with and without the aerosols in the atmosphere. Aerosol DRE can be estimated by means of radiative transfer model (RTM) simulations.

ACPD
14, 541–591, 2014

In this work the RTM libRadtran (Mayer and Kylling, 2005) was used, adopting as radiative transfer equation solver the discrete ordinate code disort (Stamnes et al., 1988) with 18 streams. The correlated-k approach of Kato (Kato et al., 1999) was used to compute the atmospheric spectral transmittance taking into account the absorption coefficients of different gases.

RTM simulations were performed at the three measurement sites in 15 min intervals for the duration of the measurement campaign, from 11:00 UTC to 13:45 UTC. The average was computed in order to obtain an estimate of the maximum radiative forcing of aerosol, which is generally observed around noon.

Atmospheric profiles of pressure, temperature, air density, ozone, oxygen, water vapor, CO_2 and NO_2 concentrations were defined by using the standard atmospheric data as defined by Anderson et al. (1986) for *Midlatitude Winter*. The vertical resolution of the profiles is 1 km from 0 to 25 km a.m.s.l., 2.5 km from 25 to 50 km a.m.s.l., and 5 km from 50 to 120 km a.m.s.l..

Optical properties of atmospheric aerosols, i.e. extinction coefficient, single scattering albedo, and moments of the phase function, were specified explicitly and calculated as reported in the previous section (Sect. 2.3).

Surface albedo values used for the simulation derive from retrievals from the MODerate Resolution Imaging Spectroradiometer (MODIS) V005 Climate Modeling Grid (CMG) Albedo Product (MCD43C3). For each site, the average value at the nearest pixel during the measurement campaign was adopted.

3 Results and discussion

We measured the BC vertical profiles to determine the BC direct radiative effect. The obtained results are discussed here in order to highlight first the BC vertical distribution in relation to the mixing height (MH, Sects. 3.1). Then, vertical profiles of aerosol optical properties are reported and discussed in Sect. 3.2 and, finally, the aerosol DRE along height is presented together with considerations on possible feedbacks on lower

ACPD
14, 541–591, 2014

troposphere (Sect. 3.3). All averaged data are reported here as mean ± mean standard deviation.

3.1 Vertical profile measurements

3.1.1 Black Carbon and aerosol profiles

The main features of BC and aerosol vertical distribution during the campaign can be highlighted considering, as a case study, the vertical profiles measured on 28 January 2010 (13:45–14:26 UTC) over TR; they are reported in Fig. 2 together with the corresponding potential temperature (T) and RH profiles.

Figure 2 highlights that the BC and the total particle number concentrations were constrained close to ground, within the first 170 m a.g.l., where a strong negative gradient of both of them was present; at the same height an evident decrease of RH (−3.5 %) and a small increase in T (+0.7 K) was observed, allowing to set the MH at 170 m.

Thus, considering changes across the MH, the BC concentration decreased going from BMH to AMH by 60.4 ± 2.3 % (from 5.63 ± 0.16 $\mu g\,m^{-3}$ to 2.23 ± 0.05 $\mu g\,m^{-3}$) and the aerosol concentration by 35.4 ± 0.2 % (from 869 ± 2 cm^{-3} to 562 ± 2 cm^{-3}). Thus, the vertical profiles reported in this case study (Fig. 2) indicates that: (1) BC and aerosol concentrations were shaped in the same way by atmospheric turbulence and constrained below the MH; (2) BC experienced a higher concentration drop at the MH than the aerosol number concentration did.

In order to better investigate these features, all the vertical profiles measured over the investigated basin valleys (TR, MI and ME) were statistically averaged for each site.

As reported in previous works (Ferrero et al., 2011a, 2012), a way to average vertical profile data by taking the daily evolution of the MH into account, is to consider the relative position of each measured data point in respect to the MH. Thus, vertical profile

ACPD
14, 541–591, 2014

were first normalized, introducing a standardized height (H_s) calculated as follows:

$$H_s = \frac{z - \mathrm{MH}}{\mathrm{MH}} \quad (11)$$

where z is the height above ground. H_s assumes a value of 0 at the MH, and values of −1 and 1 at ground-level and at twice the MH, respectively.

The MH was determined applying the gradient method (Sect. 2.2) to each aerosol particle (p-MH), T (T-MH) and RH (RH-MH) profile. Figure 3 shows excellent correlation ($R^2 > 0.9$) with linear best fits close to the ideal ones; this result illustrates the reliability and physical inter-consistence of the MH determination from different parameters. Thus, for the purpose of this work and the use of Eq. (11), we are going to refer to the MH as that derived from the aerosol concentration gradient (p-MH), hereinafter indicated simply as MH.

The average MH measured in the three site were: 142 ± 22 m (TR), 272 ± 50 m (MI) and 173 ± 42 m (ME). These values reflected a meteorological situation common for Italian basin valleys, characterized by conditions of high atmospheric stability. Reported MH values are also in agreement with those previously reported for TR and MI in Ferrero et al. (2012).

Next the standardized vertical profiles were averaged. Figure 4 shows the resulting statistical mean profiles calculated over TR, MI and ME, for both BC and aerosol number concentration; some common behaviors can be observed among the three sites:

1. At the MH ($H_s = 0$) a marked concentration drop of both BC and the whole aerosol was observed. Crossing the mixing height, BC concentrations decreased over TR by 69.1 ± 5.5 % (from 5.63 ± 0.55 $\mu g\,m^{-3}$ to 1.67 ± 0.36 $\mu g\,m^{-3}$), over MI by 66.2 ± 7.8 % (from 7.57 ± 1.28 $\mu g\,m^{-3}$ to 2.03 ± 0.34 $\mu g\,m^{-3}$) and over ME by 48.4±5.3 % (from 2.75±0.38 $\mu g\,m^{-3}$ to 1.35±0.17 $\mu g\,m^{-3}$); aerosol concentrations (from BMH to AMH) behave similarly, decreasing over TR by 46.5 ± 7.3 % (from 792 ± 58 cm^{-3} to 434 ± 71 cm^{-3}), over MI by 39.0 ± 7.3 % (from 913 ± 120 cm^{-3} to 506±50 cm^{-3}) and over ME by 23.9±4.3 % (from 427±45 cm^{-3} to 326±43 cm^{-3}),

ACPD
14, 541–591, 2014

respectively. Thus, the experimental results evidenced the crucial role played by the MH in shaping both the BC and aerosol profiles over basin-valleys; as a result elevated BC and aerosol loading was present close to the ground. Another common behavior appeared: the partial decrease of BC across the MH was always higher than the decrease measured for the aerosol number concentration; thus, the BC content of the aerosol decreased along height in all the three sites. In fact, considering not only the number concentration, but also the $PM_{2.5}$ mass concentration profiles (estimated by the OPC) and the volume concentration profiles for particles below 2.5 µm ($V_{2.5}$, calculated from OPC size distribution), the BC content in $PM_{2.5}$ ($V_{2.5}$) decreased along height by 43.2 ± 7.3 % (41.8 ± 7.5 %), 47.5 ± 7.9 % (45.8 ± 8.3 %) and 33.2 ± 4.9 % (33.0 ± 5.4 %) over TR, MI and ME, respectively, resulting in a vertical change of the BC aerosol fraction (see also Sect. 3.1.2). This is a general behaviour measured over basin valleys under atmospheric stagnant conditions and it is in agreement with BC measurements previously conducted just over MI (Ferrero et al., 2011). The importance of this behaviour is discussed in Sects. 3.2 and 3.3 as the BC fraction changes affect the aerosol optical properties (i.e. SSA) and its DRE along height.

2. Within the mixing layer itself, higher BC concentrations were found close to the ground in all the three sites (Fig. 4). In particular this ground-level layer affected the first 50–100 m of atmosphere with a BC concentration increase of +34.2 % (TR), +17.3 % (MI) and +16.1 % (ME) compared to the average BC concentration measured within the whole mixing layer. This increase of BC concentration near ground-level is related to the proximity to combustion sources (traffic, heating, industry) (Trompetter et al., 2013) and was observed for BC only and not for the particle number distribution. This further strengthens the aforementioned observation of the vertical changes in the BC aerosol fraction.

3. BC concentrations measured AMH were found quite similar over the three sites: 1.67 ± 0.36 µg m^{-3} for TR, 2.03 ± 0.34 µg m^{-3} for MI and 1.35 ± 0.17 µg m^{-3} for ME

ACPD
14, 541–591, 2014

(Fig. 4) indicating the presence of a relatively constant background BC concentration value not directly influenced in short term by the source dynamics on the ground.

As many scholars reported a large degree of uncertainty (20–50 %) of the worldwide aerosol DRE comes from a lack of knowledge about BC vertical distribution (Samset et al., 2013; Zarzycki and Bond, 2010) thus, the aforementioned results were used in Sect. 3.2 and 3.3 to assess the related vertical behavior of both aerosol optical properties and aerosol DRE over basin valleys.

3.1.2 Aerosol chemistry along height and DRH

The optical properties calculations along vertical profiles (Sects. 2.3 and 3.2) require the knowledge of the whole aerosol chemical composition along height. Thus, in addition to BC (Sect. 3.1.1), the other chemical components (ions, OM; Sect. 2.2.2) in $PM_{2.5}$ are discussed here. Figure 5 shows the aerosol chemical composition over TR, MI and ME both BMH and AMH.

As highlighted in the previous section, Fig. 5 evidences the decrease of BC fraction from BMH (8.4 ± 1.0 % over TR, 10.1 ± 2.3 % over MI and 8.6 ± 1.5 % over ME) to AMH (4.5 ± 1.2 % over TR, 5.3 ± 1.0 % over MI and 5.5 ± 1.4 % over ME).

Conversely, the OM fraction increased with height (from BMH to AMH): from 29.5 ± 3.6 % to 32.4 ± 8.4 % over TR, from 35.6 ± 8.2 % to 44.1 ± 7.4 % over MI and from 30.4 ± 5.3 % to 44.2 ± 7.3 % over ME.

This difference in the vertical behavior of BC and OM is related first to the presence of primary sources of BC within the mixing layer (Trompetter et al., 2013), but also to the possibility of greater secondary aerosol formation AMH. This is in agreement with results previously reported over the Po Valley (Ferrero et al., 2011a; Perrone et al., 2010) and also over Europe by many authors (Morgan et al., 2009; Schneider et al., 2006; Hueglin et al., 2005), who all found a lower vertical gradient for organic species.

ACPD
14, 541–591, 2014

Ionic species exhibited different behavior over the three sites. Over TR the whole ionic fraction increased ∼ 2 times going from BMH to AMH. The mass fraction of NO_3^-, SO_4^{2-} and NH_4^+ increased from 4.2 ± 1.8 %, 3.7 ± 2.6 % and 3.0 ± 1.5 % (BMH) to 11.0 ± 3.6 %, 4.2 ± 1.1 % and 4.3 ± 1.4 % (AMH), respectively. This is in agreement with recent studies (Moroni et al., 2013; Ferrero et al., 2012) which point to the presence of an aerosol aging AMH due to both condensation and coagulation.

Over MI the opposite occurred and the ionic fraction globally decreased from 40.0 ± 9.5 % (BMH) to 30.2 ± 7.2 % (AMH). This is also in agreement with previous vertical profiles conducted over MI (Ferrero et al., 2010, 2012) which instead underlined a higher role of the OM (see above) in the aerosol aging AMH over the Po Valley.

Over ME the ionic fraction decreased with height (from 23.0 ± 9.0 % BMH to 16.7 ± 2.2 % AMH) as in MI. However, while in MI and TR NO_3^- remained the most abundant species AMH, over ME SO_4^{2-} dominated. This was due to the alternating influence of both continental aerosol (enriched in SO_4^{2-}) and Po Valley aerosol, that were transported from North and South, respectively, along the direction of the ME main Valley (Sect. 2.1).

All these aspects are crucial in determining the aerosol optical properties because, as reported in Ramana et al. (2010), the ratio of BC to scattering species (i.e. SO_4^{2-}) influences the solar-absorption efficiency. Moreover, the same scattering species (i.e. SO_4^{2-} and NO_3^-) also influence the DRH at which aerosol water uptake starts, corresponding to a phase change for the aerosol water-soluble compounds which dissociate going from solid to liquid (Martin, 2000; Seinfeld and Pandis, 1998; Potukuchi and Wexler, 1995); thus DRH is therefore of fundamental importance to assess the final aerosol optical properties (Di Nicolantonio et al., 2009; Randriamiarisoa et al., 2006).

In this respect, the E-AIM Model II (Sect. 2.3.1) was applied to the H^+-NH_4^+-SO_4^{2-}-NO_3^--carboxylic acids-H_2O composition of the aerosol to accurately predict the aerosol DRH for each site both BMH and AMH. BMH values of DRH for TR, MI and ME were close each other: 64.5 %, 67.0 % and 65 %, respectively. They are in agreement with

ACPD
14, 541–591, 2014

values measured at ground level in MI by means of an Aerosol Chamber (Ferrero et al., 2013b).

Values of DRH were estimated for TR, MI and ME to be AMH 55 %, 62.5 % and 67 %, respectively. The lowest and the highest values were found over TR and ME due to an increase in the nitrate and sulfate fractions, respectively; as Potukuchi and Wexler (1995) have pointed out, an increase in the nitrate (sulfate) fraction leads to lower (higher) DRH.

All of these results were used to calculate the aerosol optical properties along vertical profiles (Sect. 3.2) following the methodology reported in Sect. 2.3.

3.2 Vertical profiles of aerosol optical properties

The vertical profiles of aerosol optical properties were calculated as reported in Sect. 2.3. In this section, the reliability of the calculated optical properties is first discussed (Sect. 3.2.1) prior to the investigation of their vertical profiles over the three sampling sites (Sect. 3.2.2).

3.2.1 AERONET comparison

The reliability of the calculated aerosol optical properties is at the basis both of the discussion of their vertical behaviour (Sect. 3.2.2) and of the aerosol DRE calculations (Sect. 3.3). Thus, this reliability was evaluated through a comparison of a set of parameters (i.e. refractive index, SSA, AOD...) independently obtained by the Aerosol Robotic Network (AERONET) at 441 nm, 657 nm and 880 nm (the only overlapping wavelenghts between this study and AERONET). Considering the location of TR, MI and ME, only three AERONET stations were available for this comparison: the Ispra site (45.80° N, 8.63° E, 235 m a.s.l., 57 km from MI site), the Davos site (46.81° N, 9.84° E, 1596 m a.s.l., 102 km and 157 km from ME and MI sites) and the Bolzano site (46.46° N, 11.33° E, 262 m a.s.l., 25 km from ME). Unfortunately, the data in Bolzano (during winter 2010) were strongly affected by local dust deposited on the photometer lens (personal

ACPD
14, 541–591, 2014

communication by the AERONET-Bolzano principal investigator) and thus, only the AERONET sites of Ispra and Davos were considered. Their data were compared with those calculated for MI, which was the nearest site. The Ispra site was used for comparison concerning the entire atmospheric column while the Davos site (1596 m a.s.l.) for the Free Troposphere (FT), due to the low MH measured over MI during the wintertime campaign (272 ± 50 m).

MI data were calculated on statistical mean profiles (Sect. 3.1.1) and we accordingly used the AERONET averaged values from 12 February to 25 February as a reference in order to assess the accuracy of our optical estimations. It is necessary to underline that, despite the averaging period is the same, the instantaneous values measured by balloon sounding and by AERONET could not have been coincident and this temporal difference may cause small differences during the comparison.

We start the comparison considering the whole atmospheric column, results are resumed in Table 2. The average columnar refractive indexes calculated in this study were 1.501(±0.003)+i0.032(±0.003) at 441 nm, 1.500(±0.004)+i0.030(±0.003) at 675 nm and 1.494(±0.004)+i0.030(±0.003) at 880 nm. They were in agreement with the AERONET-Ispra estimations: 1.415(±0.047)+i0.032(±0.009) at 441 nm, 1.418(±0.046)+i0.029(±0.006) at 675 nm and 1.425(±0.044)+i0.030(±0.007) at 870 nm. A slight overestimation of the real part (+5.6 ± 0.4 %) was present while the imaginary part was identical to the measured one.

These results validate the methodology used for the aerosol refractive index calculation (EMA mixing rule, m and ρ for pure components, hygroscopic growth) (Sect. 2.3.1); moreover, validation of the refractive index m is crucial as it is at the basis of the optical calculation both during the OPC size distribution correction and during the Mie calculation (in which the corrected size distribution is itself an important input parameter).

Thus, as a second control, the corrected and interpolated aerosol size distribution was compared to that retrieved by AERONET-Ispra: the calculated accumulation mode geometric mean diameter (D_g: 0.204 ± 0.010 µm) and the geometric standard deviation (σ_g: 1.560 ± 0.060) agreed very well with AERONET-Ispra (D_g: 0.206 ± 0.016 µm, σ_g:

ACPD
14, 541–591, 2014

1.552 ± 0.045; Table 2) allowing, together with the aforementioned validation of m, to accurately estimate the profiles of optical properties using the Mie theory.

The third step was to consider the calculated optical properties along vertical profiles. The calculated SSA (0.857±0.013 at 441 nm, 0.846±0.011 at 675 nm and 0.812±0.012 at 880 nm) was found +8.0±1.2 % higher than that of AERONET-Ispra (0.812±0.028 at 441 nm, 0.778±0.028 at 675 nm and 0.740±0.034 at 870 nm), similarly for the Aerosol Optical Depth (AOD; Table 2). The absorption Optical Depth (AOD_{Abs}; Table 2) was instead very close to the AERONET-Ispra values. The values of SSA, AOD and AOD_{Abs} are consistent with the slight overestimation of the real part of the refractive index.

From the wavelength dependence of AOD and AOD_{Abs} the corresponding columnar Ångström exponents were calculated: 1.56 and 1.24; they were close to the AERONET-Ispra estimation: 1.49 ± 0.12 and 1.02 ± 0.07 respectively.

Finally, the columnar aerosol phase function $P(\theta)$ was compared with that estimated by AERONET-Ispra, as it is required for the aerosol DRE calculation (Sect. 2.4); Fig. 6a shows this comparison for λ = 675 nm and, for all wavelenghts, a high correlation was found (R^2 = 0.988).

As a last control step, the FT properties were also investigated comparing data above 1 km (derived as reported in Sect. 2.2.2), with AERONET-Davos data.

Table 3 resumes the results of this comparison underlying that the FT properties were in agreement with tha AERONET-Davos measurements, especially for what concern the AOD_{Abs}; the small differences encountered for other parameters (i.e. a slight overestimation of n: +2.8 ± 0.9 %) were considered negligible.

Thus, the MI data were considered reliable as they were in good agreement with the columnar AERONET Ispra and Davos data. This result is very important as it validated the procedure used for the optical properties calculation (Sect. 2.3) allowing its application also along the vertical profiles measured over TR and ME as well.

ACPD
14, 541–591, 2014

3.2.2 Comparison with aethalometer data

In the previous section, a good agreement between the calculated optical properties and the properties measured by the AERONET network was evidenced.

However, in order to calculate the aerosol DRE at high spatial resolution along vertical profiles (Sect. 2.4) not only a right estimation of the columnar-averaged parameters, but also a correct shaping of them along vertical profiles is needed. This requirement is necessary to avoid the presence of compensatory effects along profiles and to perform a right estimation of the radiation absorbed in each atmospheric layer (Sects. 2.4 and 3.3).

Thus, in addition to the comparison with AERONET (columnar agreement), a detailed comparison along vertical profiles is also necessary.

For this purpose the b_{abs} measured by the micro-Aeth® AE51 at 880 nm was compared along vertical profiles with that calculated over TR, MI and ME for the same wavelength (Fig. 6b); results showed an excellent agreement ($b_{abs\_calc} = 1.001 \cdot b_{abs\_AE51} - 0.157$, $R^2 = 0.996$, RMSE = 0.87 Mm^{-1}) validating the Mie calculation of the b_{abs} vertical profiles.

Moreover, measurements performed close to the ground by the micro-Aeth® AE51 at 880 nm in ME were compared with that carried out at ground with the 7-λ Aethalometer AE31 (Sect. 2.2). Only AE31 data that were timely coincident with balloon profiles were considered. The averaged BC and b_{abs} measured by the AE51 were $2.75 \pm 0.38\ \mu g\,m^{-3}$ and $16.8 \pm 2.3\ M\,m^{-1}$ in keeping with the AE31 data: $2.74 \pm 0.10\ \mu g\,m^{-3}$ and 18.7 ± 0.7 Mm^{-1}, respectively. Moreover, the 7-λ AE31 Aethalometer allowed the comparison of the ground-level absorption Ångström exponent (1.43 ± 0.03) with that obtained by Mie calculation: 1.36 ± 0.01.

These results conclude the validation procedure allowing to discuss the aerosol optical properties behavior over the three sites and to calculate DRE profiles in a reliable way.

ACPD
14, 541–591, 2014

3.2.3 Optical properties

The vertical behavior of aerosol optical properties was similar for all the investigated wavelengths thus, in this section, we report and discuss results at 675 nm which represent the central wavelength with respect to the wavelength range used for the DRE calculation (Sect. 2.4).

The calculated optical properties (at 675 nm) along height over TR, MI and ME are reported in Fig. 7. Over the three sites, both b_{sca} and b_{abs} (and thus b_{ext}) experienced higher values BMH. For b_{abs} the highest values were found close to the ground (within the first 50–100 m) with an average increase (compared to the average mixing layer value) of +44.9 % (TR), +19.8 % (MI) and +21.9 % (ME). This ground-level increase is associated with the aerosol chemical composition change with height (Sect. 3.1.1) and is related to the proximity of BC sources (traffic, heating, industry).

Considering changes across the MH ($H_s = 0$), b_{sca} and b_{abs} decreased strongly going from BMH to AMH. On average b_{sca} and b_{abs} decreased (from BMH to AMH) over TR by 43.1 ± 3.0 % (from $157.6 \pm 2.3\,Mm^{-1}$ to $89.7 \pm 4.5\,Mm^{-1}$ for b_{sca}) and by 58.8 ± 4.5 % (from 45.3 ± 4.6 Mm^{-1} to $18.7 \pm 0.7\,Mm^{-1}$ for b_{abs}). Over MI their decrease was of 61.2 ± 3.1 % (from $253.3 \pm 2.0\,Mm^{-1}$ to $98.2 \pm 7.7\,Mm^{-1}$ for b_{sca}) and by 71.3 ± 3.0 % (from 69.0 ± 4.0 Mm^{-1} to $19.8 \pm 1.7\,Mm^{-1}$ for b_{abs}) and over ME the same happened with a decrease of 23.5 ± 0.8 % (from $85.1 \pm 0.7\,Mm^{-1}$ to $65.1 \pm 0.4\,Mm^{-1}$ for b_{sca}) and by 47.6 ± 2.5 % (from 23.8 ± 1.0 Mm^{-1} to $12.4 \pm 0.2\,Mm^{-1}$ for b_{abs}), respectively.

The highest values of b_{sca} and b_{abs} BMH were observed in MI, followed by TR and then by ME which reflects the pollution level over the three sites described in Sect. 3.1.1. Conversely, AMH the background pollutant concentrations were similar for all three sites (Sect. 3.1.1) resulting in different b_{sca} and b_{abs} gradients across the mixing height in TR, MI and ME.

However, the most important result that can be observed is the higher decrease experienced at the MH by b_{abs}, compared to b_{sca}. As a consequence, the SSA in-

ACPD
14, 541–591, 2014

creased along height (from BMH to AMH) over the three sites by +5.7 ± 2.0 % over TR (from 0.781 ± 0.014 to 0.825± 0.004), +4.9 ± 2.2 % over MI (from 0.787 ± 0.010 to 0.826 ± 0.014) and by +7.4 ± 1.0 % over ME (from 0.783 ± 0.007 to 0.840 ± 0.002).

This can be interpreted in relation to the aerosol chemical composition changes with height reported in Sects. 3.1.1 and 3.1.2: the BC aerosol fraction decreased and a corresponding increase in scattering species (i.e. ionic compounds) was present AMH. This result is of a great importance as, first, it appears as a general behavior over the three investigated sites and, second, this behavior affects the DRE effect and the heating rate due to aerosol along height, as it will be shown in Sect. 3.3.

Finally, due to the consideration that the DRE calculation (Sect. 2.4) also requires FT aerosol optical properties as input data, we also report here their values: b_{sca} and b_{abs} were 1.9 ± 0.9 Mm^{-1} and 0.2 ± 0.1 Mm^{-1}, respectively and, as a consequences, the FT SSA was 0.932 ± 0.003, higher than in the residual layer, as expected due to the lower BC content with height. We remind that the FT validation was yet discussed in Sect. 3.2.1 (Table 3).

3.3 DRE profiles, heating rate and potential feedbacks

Instantaneous aerosol DRE profiles were calculated over the whole solar spectrum (0.25–3 µm) from 11:00 UTC to 13:45 UTC (temporal range of the averaged profiles over TR, MI and ME) to estimate the maximum DRE effect at noon (Sect. 2.4).

Below the MH, the highest DRE was observed over MI (−51.0 ± 2.6 Wm^{-2}) followed by TR (−39.7±0.7 Wm^{-2}) and ME (−29.5±0.5 Wm^{-2}). Above the MH, MI and TR experienced a similar forcing (−29.7 ± 1.4 Wm^{-2} and −29.6 ± 1.0 Wm^{-2}, respectively) higher than that observed over ME (−19.0±0.7 Wm^{-2}). In the FT, over the three sites, the DRE was similar: −5.6 ± 0.3 Wm^{-2} (MI), −6.3 ± 0.2 Wm^{-2} (TR) and −6.1 ± 0.3 Wm^{-2} (ME) indicating a net cooling effect of the aerosol on the earth-atmospheric system and in keeping with values reported in Perrone and Bergamo (2011) and in Saha et al. (2008).

The difference between the DRE at the top and the bottom of the atmosphere indicated that a significant amount of energy was absorbed into the atmosphere heating

ACPD
14, 541–591, 2014

it. Thus, in order to quantify this phenomenon and to describe its vertical behavior at high vertical resolution, the aerosol DRE profiles were used to compute the radiative power density absorbed by the aerosol within each atmospheric layer (ΔF_{ATM}), as the difference of the aerosol DRE at the top and the bottom of each atmospheric layer. Figure 8 reports ΔF_{ATM} profiles over TR, MI and ME; since the wintertime aerosol absorption was due to the presence of BC, ΔF_{ATM} represented the atmospheric DRE of BC (BC-DRE).

The highest ΔF_{ATM} was observed BMH over MI ($2.5 \pm 0.2\,W\,m^{-2}$) followed by TR ($0.7 \pm 0.1\,W\,m^{-2}$) and ME ($0.5 \pm 0.1\,W\,m^{-2}$); the same order was observed considering AMH data: higher values were found over MI ($1.2 \pm 0.1\,W\,m^{-2}$) followed by TR ($0.5 \pm 0.1\,W\,m^{-2}$) and ME ($0.4 \pm 0.1\,W\,m^{-2}$). They were in agreement with the BC concentrations and the BC aerosol fractions measured within the mixing layer and above it (in the residual layer) over the three sites (Sect. 3.1.1). Despite the observed differences among TR, MI and ME, a common feature occurred: ΔF_{ATM} decreased with height, with respect to the MH altitude, by 51.7 ± 4.9 % over MI, 33.3 ± 4.0 % over TR and 2.7 ± 0.2 % over ME even if over MI and TR, this phenomenon was more intense and a sharp change in the BC-DRE was observed at the MH ($H_s = 0$).

Most of the BC-DRE occurred within the mixing layer, in agreement with the BC pollution loading in basin valleys, especially over the most urbanized and industrialized sites. This behavior has an important feature, as the ΔF_{ATM} induces an instantaneous heating rate (HR) in the lower troposphere that can be computed as follows:

$$\frac{\partial T}{\partial t} = \frac{g}{C_p}\frac{\Delta F_{ATM}}{\Delta P} \tag{12}$$

where $\partial T/\partial t$ represents the instantaneous heating rate ($K\,day^{-1}$) of each atmospheric layer, g is the acceleration due to gravity, C_p ($1005\,J\,kg^{-1}\,K^{-1}$) is the isobaric specific heat of dry air, ΔP is the absolute pressure difference between the top and the bottom of each atmospheric layer.

ACPD
14, 541–591, 2014

The calculated heating rate profiles are reported in Fig. 8 together with ΔF_{ATM} profiles: due to the high vertical resolution of balloon soundings, the heating dynamics across the MH are well characterized. Particularly, the highest degree of instantaneous heating rate was observed BMH: $7.5 \pm 1.1\,K\,day^{-1}$ over MI, $3.9 \pm 0.1\,K\,day^{-1}$ over TR and $2.1 \pm 0.1\,K\,day^{-1}$ over ME. Above the MH values were lower, especially over MI ($3.4 \pm 0.1\,K\,day^{-1}$) and TR ($2.6 \pm 0.1\,K\,day^{-1}$), while over ME the heating rate was at the same level ($2.0 \pm 0.1\,K\,day^{-1}$) that BMH with a more complicated vertical profile.

The higher heating rate values observed BMH should turn into a weakening of the ground-based thermal inversion, which are common in these basin valleys (Ferrero et al., 2012).

It would be helpful to be able to describe the potential feedbacks induced by the atmospheric heating rate by a simple parameter. We propose here the use of the heating rate vertical gradien ($K\,day^{-1}\,km^{-1}$) as a proxy of the feedback potential (HERFPO: HEating Rate Feedback POtential). The HERFPO represents the atmospheric thermal lapse rate that would take place if the forcing induced by the instantaneous HR profile would last all day.

Thus, the HERFPO was calculated along the HR profiles (from the bottom to the top) over each measuring site: $-6.8\,K\,day^{-1}\,km^{-1}$ over MI, $-6.0\,K\,day^{-1}\,km^{-1}$ over TR and $-0.5\,K\,day^{-1}\,km^{-1}$ over ME.

If we compare the previous data with the atmospheric dry adiabatic lapse rate ($-10\,K\,km^{-1}$) we observe that the vertical HR had really the potential to result in a negative feedback promoting an increase of the atmospheric dispersal conditions, by weakening the ground-based thermal inversions, especially over MI and TR.

The aforementioned results are of great importance as they highlight a common behaviour along height over Italian basin valleys and could be considered in a first step of a general validity under atmospheric stagnant conditions.

ACPD
14, 541–591, 2014

4 Conclusions

Vertical profiles of BC and aerosol number-size distribution were measured over three Italian basin valleys (Po Valley, Terni Valley and Passiria Valley) and allowed to characterize the aerosol and BC dispersion under similar orographic conditions. Changes of the BC concentrations and BC aerosol fraction along heigh were related with variations in aerosol optical properties, radiative forcing and heating rate.

Measurements were conducted during week-long wintertime campaigns and the vertical aerosol properties were obtained by means of a tethered balloon-based moving platform (fitted with a micro-Aethalometer, an OPC, a cascade impactor and a meteorological station) while aerosol chemical composition was determined analysing $PM_{2.5}$ samples collected at different height.

Results from the measured vertical profiles allowed to clearly identify the mixing height (MH), which was characterized by a strong vertical concentration gradient of both BC (range: -48.4 ± 5.3 % to -69.1 ± 5.5 %) and aerosol (range: -23.9 ± 4.3 % to -46.5 ± 7.3 %). Above the MH, the percentage decrease of BC was higher than that measured for aerosol and thus, the BC fraction of aerosol fell (range: -33.2 ± 4.9 % to -47.5 ± 7.9 %) while a shallow BC layer of higher concentrations (range: +16.1 % to +34.2 %) was found close to the ground, in the first 50–100 m of the atmosphere, due to the proximity of BC sources. These behaviours caused a change in the optical absorption properties of the aerosol at different heights that was quantified applying Mie theory to aerosol data. Before this step, the aerosol refractive index was calculated using the effective medium approximation applied to aerosol chemical composition and the OPC number-size distribution was corrected for the ambient aerosol refractive index. Results were validated with AERONET data and evidenced an increase of the Single Scattering Albedo with height (range: $+4.9 \pm 2.2$ % to $+7.4 \pm 1.0$ %).

The effect of optical properties changes with height was assessed using a radiative transfer model (libRadtran) from which vertical profiles of direct aerosol radiative forcing, atmospheric absorption and heating rate were calculated. The highest atmo-

ACPD
14, 541–591, 2014

spheric absorption was observed below the mixing height (range: $+0.5 \pm 0.1\,W\,m^{-2}$ to $+2.5 \pm 0.2\,W\,m^{-2}$) and was responsible of a heating rate characterized by a vertical negative gradient (range: $-0.5\,K\,day^{-1}\,km^{-1}$ to $-6.8\,K\,day^{-1}\,km^{-1}$). Thus, the behaviour of BC loaded below the MH resulted in a negative feedback able to promote an increase of the atmospheric dispersal conditions.

The obtained results were similar over the three sites and pointed towards a common aerosol dynamics over basin valleys characterized by similar atmospheric stagnant conditions. These data represent the first high resolution vertical profile of aerosol radiative forcing and heating rate obtained over Italy and Europe allowing to describe with detail the radiative forcing induced by BC (and aerosol) in the lower troposphere, across the mixing layer and within it, where the antroposphere is located.

Acknowledgements. We thank Fondazione CARIT di Terni e Narni, ARPA Umbria, EURAC, and the SINOPIAE project (funded by Lombardy Region) for financial support to this research. We are grateful to the Physical and chemical laboratory of the autonomous province of Bolzano/Bozen for the logistic support during the campaign in Merano.

References

Ackerman, T. P. and Toon, O. B.: Absorption of visible radiation in atmosphere containing mixtures of absorbing and nonabsorbing particles: erratum, Appl. Optics, 21, 758–758, doi:10.1364/AO.21.000758, 1982.

Arnott, W. P., Hamasha, K., Moosmüller, H., Sheridan, P. J., and Ogren, J. A.: Towards aerosol light-absorption measurements with a 7-wavelength aethalometer: evaluation with a photoacoustic instrument and 3-wavelength nephelometer, Aerosol Sci. Tech., 39, 17–29, doi:10.1080/027868290901972, 2005.

Babu, S. S., Sreekanth, V., Moorthy, K. K., Mohan, M., Kirankumar, N. V. P., Subrahamanyam, D. B., Gogoi, M. M., Kompalli, S. K., Beegum, N., Chaubey, J. P., Kumar, V. H. A., and Manchanda, R. K.: Vertical profiles of aerosol black carbon in the atmospheric boundary layer over a tropical coastal station: perturbations during an annular solar eclipse, Atmos. Res., 99, 471–478, doi:10.1016/j.atmosres.2010.11.019, 2011.

ACPD
14, 541–591, 2014

Bond, T. C. and Bergstrom, R. W.: Light absorption by carbonaceous particles: an investigative review, Aerosol Sci. Tech., 40, 27–67, doi:10.1080/02786820500421521, 2006.

Bond, T. C., Doherty, S. J., Fahey, D. W., Forster, P. M., Berntsen, T., Deangelo, B. J., Flanner, M. G., Ghan, S., Kärcher, B., Koch, D., Kinne, S., Kondo, Y., and Quinn, P. K.: Bounding the role of black carbon in the climate system?: a scientific assessment, J. Geophys. Res., 118, 1–173, doi:10.1002/jgrd.50171, 2013.

Cape, J. N., Coyle, M., and Dumitrean, P.: The atmospheric lifetime of black carbon, Atmos. Environ., 59, 256–263, doi:10.1016/j.atmosenv.2012.05.030, 2012.

Carbone, C., Decesari, S., Mircea, M., Giulianelli, L., Finessi, E., Rinaldi, M., Fuzzi, S., Marinoni, A., Duchi, R., Perrino, C., Sargolini, T., Vardè, M., Sprovieri, F., Gobbi, G. P., Angelini, F., and Facchini, M. C.: Size-resolved aerosol chemical composition over the Italian Peninsula during typical summer and winter conditions, Atmos. Environ., 44, 5269–5278, doi:10.1016/j.atmosenv.2010.08.008, 2010.

Chakrabarty, R. K., Garro, M. A., Wilcox, E. M., and Moosmüller, H.: Strong radiative heating due to wintertime black carbon aerosols in the Brahmaputra River Valley, Geophys. Res. Lett., 39, L09804, doi:10.1029/2012GL051148, 2012.

Chazette, P. and Liousse, C.: A case study of optical and chemical ground apportionment for urban aerosols in Thessaloniki, Atmos. Environ., 35, 2497–2506, doi:10.1016/S1352-2310(00)00425-8, 2001.

Clegg, S. L., Brimblecombe, P., and Wexler, A. S.: Thermodynamic model of the system H^+ – NH_4^+ – SO_4^{2-} – NO_3 – H_2O at tropospheric temperatures, J. Phys. Chem. A, 5639, 2137–2154, 1998.

Crosbie, A. L. and Davidson, G. W.: Approximations to the scattering phase function, J. Quant. Spectrosc. Radiat. Transfer, 33, 391–409, 1985.

Deshler, T.: Thirty years of in situ stratospheric aerosol size distribution measurements from Laramie, Wyoming (41° N), using balloon-borne instruments, J. Geophys. Res., 108, 4167, doi:10.1029/2002JD002514, 2003.

Emili, E., Popp, C., Petitta, M., Riffler, M., Wunderle, S., and Zebisch, M.: PM_{10} remote sensing from geostationary SEVIRI and polar-orbiting MODIS sensors over the complex terrain of the European Alpine region, Remote Sens. Environ., 114, 2485–2499, doi:10.1016/j.rse.2010.05.024, 2010.

Ferrero, L., Cappelletti, D., Moroni, B., Sangiorgi, G., Perrone, M. G., Crocchianti, S., and Bolzacchini, E.: Wintertime aerosol dynamics and chemical composition across the mixing

ACPD
14, 541–591, 2014

layer over basin valleys, Atmos. Environ., 56, 143–153, doi:10.1016/j.atmosenv.2012.03.071, 2012.

Ferrero, L., Mocnik, G., Ferrini, B. S., Perrone, M. G., Sangiorgi, G., and Bolzacchini, E.: Vertical profiles of aerosol absorption coefficient from micro-Aethalometer data and Mie calculation over Milan., Sci. Total Environ., 409, 2824–37, doi:10.1016/j.scitotenv.2011.04.022, 2011a.

Ferrero, L., Perrone, M. G., Petraccone, S., Sangiorgi, G., Ferrini, B. S., Lo Porto, C., Lazzati, Z., Cocchi, D., Bruno, F., Greco, F., Riccio, A., and Bolzacchini, E.: Vertically-resolved particle size distribution within and above the mixing layer over the Milan metropolitan area, Atmos. Chem. Phys., 10, 3915–3932, doi:10.5194/acp-10-3915-2010, 2010.

Ferrero, L., Riccio, A., Perrone, M. G., Sangiorgi, G., Ferrini, B. S., and Bolzacchini, E.: Mixing height determination by tethered balloon-based particle soundings and modeling simulations, Atmos. Res., 102, 145–156, doi:10.1016/j.atmosres.2011.06.016, 2011b.

Ferrero, L., Sangiorgi, G., Ferrini, B. S., Perrone, M. G., Moscatelli, M., D'Angelo, L., Rovelli, G., Ariatta, A., Truccolo, R., and Bolzacchini, E.: Aerosol corrosion prevention and energy-saving strategies in the design of green data centers., Environ. Sci. Technol., 47, 3856–64, doi:10.1021/es304790f, 2013a.

Ferrero, L., D'Angelo, L., Rovelli, G., Sangiorgi, G., Perrone, M. G., Moscatelli, M., Casati, M., and Bolzacchini, E.: Determination of Aerosol Deliquescence and Crystallization Relative Humidity for Energy Saving in Free-Cooled Data Centers, Int. J. Environ. Sci. Technol., submitted, 2013b.

Fierz-Schmidhauser, R., Zieger, P., Gysel, M., Kammermann, L., DeCarlo, P. F., Baltensperger, U., and Weingartner, E.: Measured and predicted aerosol light scattering enhancement factors at the high alpine site Jungfraujoch, Atmos. Chem. Phys., 10, 2319–2333, doi:10.5194/acp-10-2319-2010, 2010.

Guyon, P., Boucher, O., Graham, B., Beck, J., Mayol-Bracero, O. L., Roberts, G. C., Maenhaut, W., Artaxo, P., and Andreae, M. O.: Refractive index of aerosol particles over the Amazon tropical forest during LBA-EUSTACH 1999, J. Aerosol Sci., 34, 883–907, doi:10.1016/S0021-8502(03)00052-1, 2003.

Heim, M., Mullins, B. J., Umhauer, H., and Kasper, G.: Performance evaluation of three optical particle counters with an efficient "multimodal" calibration method, J. Aerosol Sci., 39, 1019–1031, doi:10.1016/j.jaerosci.2008.07.006, 2008.

ACPD
14, 541–591, 2014

Hess, M., Koepke, P., and Schult, I.: Optical properties of aerosols and clouds: the software package OPAC, B. Am. Meteorol. Soc., 79, 831–844, doi:10.1175/1520-0477(1998)079<0831:OPOAAC>2.0.CO; 2, 1998.

Heyder, J. and Gebhart, J.: Optimization of response functions of light scattering instruments for size evaluation of aerosol particles., Appl. Optics, 18, 705–711, http://www.ncbi.nlm.nih.gov/pubmed/20208803, 1979.

Hueglin, C., Gehrig, R., Baltensperger, U., Gysel, M., Monn, C., and Vonmont, H.: Chemical characterisation of $PM_{2.5}$, PM_{10} and coarse particles at urban, near-city and rural sites in Switzerland, Atmos. Environ., 39, 637–651, doi:10.1016/j.atmosenv.2004.10.027, 2005.

Jacobson, M. Z.: Strong radiative heating due to the mixing state of black carbon in atmospheric aerosols, Nature, 409, 695–697, doi:10.1038/35055518, 2001.

Lesins, G., Chylek, P., and Lohmann, U.: A study of internal and external mixing scenarios and its effect on aerosol optical properties and direct radiative forcing, J. Geophys. Res., 107, 4094, doi:10.1029/2001JD000973, 2002.

Liu, Y. and Daum, P. H.: Relationship of refractive index to mass density and self-consistency of mixing rules for multicomponent mixtures like ambient aerosols, J. Aerosol Sci., 39, 974–986, doi:10.1016/j.jaerosci.2008.06.006, 2008.

Ma, X., Lu, J. Q., Brock, R. S., Jacobs, K. M., Yang, P., and Hu, X.-H.: Determination of complex refractive index of polystyrene microspheres from 370 to 1610 nm, Phys. Med. Biol., 48, 4165–72, http://www.ncbi.nlm.nih.gov/pubmed/14727759, 2003.

Maletto, A., McKendry, I. G., and Strawbridge, K. B.: Profiles of particulate matter size distributions using a balloon-borne lightweight aerosol spectrometer in the planetary boundary layer, Atmos. Environ., 37, 661–670, doi:10.1016/S1352-2310(02)00860-9, 2003.

Martin, S. T.: Phase transitions of aqueous atmospheric particles, Chem. Rev., 100, 3403–3454, http://www.ncbi.nlm.nih.gov/pubmed/11777428, 2000.

McMeeking, G. R., Hamburger, T., Liu, D., Flynn, M., Morgan, W. T., Northway, M., Highwood, E. J., Krejci, R., Allan, J. D., Minikin, A., and Coe, H.: Black carbon measurements in the boundary layer over western and northern Europe, Atmos. Chem. Phys., 10, 9393–9414, doi:10.5194/acp-10-9393-2010, 2010.

Morgan, W. T., Allan, J. D., Bower, K. N., Capes, G., Crosier, J., Williams, P. I., and Coe, H.: Vertical distribution of sub-micron aerosol chemical composition from North-Western Europe and the North-East Atlantic, Atmos. Chem. Phys., 9, 5389–5401, doi:10.5194/acp-9-5389-2009, 2009.

ACPD
14, 541–591, 2014

Moroni, B., Cappelletti, D., Marmottini, F., Scardazza, F., Ferrero, L., and Bolzacchini, E.: Integrated single particle-bulk chemical approach for the characterization of local and long range sources of particulate pollutants, Atmos. Environ., 50, 267–277, doi:10.1016/j.atmosenv.2011.12.022, 2012.

Moroni, B., Ferrero, L., Crocchianti, S., Perrone, M. G., Sangiorgi, G., Bolzacchini, E., and Cappelletti, D.: Aerosol dynamics upon Terni basin (Central Italy): results of integrated vertical profile measurements and electron microscopy analyses, Rendiconti Lincei, 24, 319–328, doi:10.1007/s12210-013-0230-8, 2013.

Pathak, R.: Characteristics of aerosol acidity in Hong Kong, Atmos. Environ., 38, 2965–2974, doi:10.1016/j.atmosenv.2004.02.044, 2004.

Perrone, M. G., Gualtieri, M., Consonni, V., Ferrero, L., Sangiorgi, G., Longhin, E., Ballabio, D., Bolzacchini, E., and Camatini, M.: Particle size, chemical composition, seasons of the year and urban, rural or remote site origins as determinants of biological effects of particulate matter on pulmonary cells., Environ. Pollut., 176, 215–27, doi:10.1016/j.envpol.2013.01.012, 2013.

Perrone, M. G., Gualtieri, M., Ferrero, L., Lo Porto, C., Udisti, R., Bolzacchini, E., and Camatini, M.: Seasonal variations in chemical composition and in vitro biological effects of fine PM from Milan, Chemosphere, 78, 1368–77, doi:10.1016/j.chemosphere.2009.12.071, 2010.

Perrone, M. G., Larsen, B. R., Ferrero, L., Sangiorgi, G., De Gennaro, G., Udisti, R., Zangrando, R., Gambaro, A. and Bolzacchini, E.: Sources of high $PM_{2.5}$ concentrations in Milan, Northern Italy: molecular marker data and CMB modelling., Sci. Total Environ., 414, 343–55, doi:10.1016/j.scitotenv.2011.11.026, 2012.

Perrone, M. R. and Bergamo, A.: Direct radiative forcing during Sahara dust intrusions at a site in the Central Mediterranean: anthropogenic particle contribution, Atmos. Res., 101, 783–798, doi:10.1016/j.atmosres.2011.05.011, 2011.

Pesava, P., Horvath, H., and Kasahara, M.: A local optical closure experiment in Vienna, J. Aerosol Sci., 32, 1249–1267, doi:10.1016/S0021-8502(01)00053-2, 2001.

Potukuchi, S. and Wexler, A. S.: Solid-aqueous-phase transitions atmospheric aerosols, II. Acidic solutions, Atmos. Environ., 29, 3357–3364, 1995.

Ramana, M. V, Ramanathan, V., Kim, D., Roberts, G. C., and Corrigan, C. E.: Albedo, atmospheric solar absorption and heating rate measurements with stacked UAVs, Q. J. Roy. Meteor. Soc., 1931, 1913–1931, doi:10.1002/qj, 2007.

ACPD
14, 541–591, 2014

Ramana, M. V., Ramanathan, V., Feng, Y., Yoon, S.-C., Kim, S.-W., Carmichael, G. R., and Schauer, J. J.: Warming influenced by the ratio of black carbon to sulphate and the black-carbon source, Nat. Geosci., 3, 542–545, doi:10.1038/ngeo918, 2010.

Ramanathan, V. and Feng, Y.: Air pollution, greenhouse gases and climate change: Global and regional perspectives, Atmos. Environ., 43, 37–50, doi:10.1016/j.atmosenv.2008.09.063, 2009.

Randriamiarisoa, H., Chazette, P., Couvert, P., Sanak, J., and Mégie, G.: Relative humidity impact on aerosol parameters in a Paris suburban area, Atmos. Chem. Phys., 6, 1389–1407, doi:10.5194/acp-6-1389-2006, 2006.

Raut, J.-C. and Chazette, P.: Vertical profiles of urban aerosol complex refractive index in the frame of ESQUIF airborne measurements, Atmos. Chem. Phys., 8, 901–919, doi:10.5194/acp-8-901-2008, 2008.

Rees, S. L., Robinson, A. L., Khlystov, A., Stanier, C. O., and Pandis, S. N.: Mass balance closure and the Federal Reference Method for $PM_{2.5}$ in Pittsburgh, Pennsylvania, Atmos. Environ., 38, 3305–3318, doi:10.1016/j.atmosenv.2004.03.016, 2004.

Rodríguez, S., Van Dingenen, R., Putaud, J.-P., Dell'Acqua, A., Pey, J., Querol, X., Alastuey, A., Chenery, S., Ho, K.-F., Harrison, R., Tardivo, R., Scarnato, B., and Gemelli, V.: A study on the relationship between mass concentrations, chemistry and number size distribution of urban fine aerosols in Milan, Barcelona and London, Atmos. Chem. Phys., 7, 2217–2232, doi:10.5194/acp-7-2217-2007, 2007.

Safai, P. D., Raju, M. P., Maheshkumar, R. S., Kulkarni, J. R., Rao, P. S. P., and Devara, P. C. S.: Vertical profiles of black carbon aerosols over the urban locations in South India, Sci. Total Environ., 431, 323–31, doi:10.1016/j.scitotenv.2012.05.058, 2012.

Saha, A., Mallet, M., Roger, J. C., Dubuisson, P., Piazzola, J., and Despiau, S.: One year measurements of aerosol optical properties over an urban coastal site: effect on local direct radiative forcing, Atmos. Res., 90, 195–202, doi:10.1016/j.atmosres.2008.02.003, 2008.

Samset, B. H., Myhre, G., Schulz, M., Balkanski, Y., Bauer, S., Berntsen, T. K., Bian, H., Bellouin, N., Diehl, T., Easter, R. C., Ghan, S. J., Iversen, T., Kinne, S., Kirkevåg, A., Lamarque, J.-F., Lin, G., Liu, X., Penner, J. E., Seland, Ø., Skeie, R. B., Stier, P., Takemura, T., Tsigaridis, K., and Zhang, K.: Black carbon vertical profiles strongly affect its radiative forcing uncertainty, Atmos. Chem. Phys., 13, 2423–2434, doi:10.5194/acp-13-2423-2013, 2013.

Sangiorgi, G., Ferrero, L., Perrone, M. G., Bolzacchini, E., Duane, M., and Larsen, B. R.: Vertical distribution of hydrocarbons in the low troposphere below and above the mixing

ACPD
14, 541–591, 2014

height: Tethered balloon measurements in Milan, Italy, Environ. Pollut., 159, 3545–3552, doi:10.1016/j.envpol.2011.08.012, 2011.

Schmid, O., Artaxo, P., Arnott, W. P., Chand, D., Gatti, L. V., Frank, G. P., Hoffer, A., Schnaiter, M., and Andreae, M. O.: Spectral light absorption by ambient aerosols influenced by biomass burning in the Amazon Basin. I: Comparison and field calibration of absorption measurement techniques, Atmos. Chem. Phys., 6, 3443–3462, doi:10.5194/acp-6-3443-2006, 2006.

Schneider, J., Hings, S. S., Nele Hock, B., Weimer, S., Borrmann, S., Fiebig, M., Petzold, A., Busen, R., and Kärcher, B.: Aircraft-based operation of an aerosol mass spectrometer: measurements of tropospheric aerosol composition, J. Aerosol Sci., 37, 839–857, doi:10.1016/j.jaerosci.2005.07.002, 2006.

Schumann, T.: On the use of a modified clean-room optical particle counter for atmosperic aerosols at high relative humidity, Atmos. Res., 25, 499–520, doi:10.1016/0169-8095(90)90035-B, 1990.

Schwarz, J. P., Gao, R. S., Fahey, D. W., Thomson, D. S., Watts, L. A., Wilson, J. C., Reeves, J. M., Darbeheshti, M., Baumgardner, D. G., Kok, G. L., Chung, S. H., Schulz, M., Hendricks, J., Lauer, A., Kärcher, B., Slowik, J. G., Rosenlof, K. H., Thompson, T. L., Langford, A. O., Loewenstein, M., and Aikin, K. C.: Single-particle measurements of midlatitude black carbon and light-scattering aerosols from the boundary layer to the lower stratosphere, J. Geophys. Res., 111, D16207, doi:10.1029/2006JD007076, 2006.

Stier, P., Seinfeld, J. H., Kinne, S., and Boucher, O.: Aerosol absorption and radiative forcing, Atmos. Chem. Phys., 7, 5237–5261, doi:10.5194/acp-7-5237-2007, 2007.

Subramanian, R., Donahue, N. M., Bernardo-Bricker, A., Rogge, W. F., and Robinson, A. L.: Insights into the primary–secondary and regional–local contributions to organic aerosol and $PM_{2.5}$ mass in Pittsburgh, Pennsylvania, Atmos. Environ., 41, 7414–7433, doi:10.1016/j.atmosenv.2007.05.058, 2007.

Trompetter, W. J., Grange, S. K., Davy, P. K., and Ancelet, T.: Vertical and temporal variations of black carbon in New Zealand urban areas during winter, Atmos. Environ., 75, 179–187, doi:10.1016/j.atmosenv.2013.04.036, 2013.

Weingartner, E., Saathoff, H., Schnaiter, M., Streit, N., Bitnar, B., and Baltensperger, U.: Absorption of light by soot particles: determination of the absorption coefficient by means of aethalometers, J. Aerosol Sci., 34, 1445–1463, doi:10.1016/S0021-8502(03)00359-8, 2003.

ACPD
14, 541–591, 2014

Zarzycki, C. M. and Bond, T. C.: How much can the vertical distribution of black carbon affect its global direct radiative forcing?, Geophys. Res. Lett., 37, L20807, doi:10.1029/2010GL044555, 2010.

Zhang, Y., Seigneur, C., Seinfeld, J. H., Jacobson, M., Clegg, S. L., and Binkowski, F. S.: A comparative review of inorganic aerosol thermodynamic equilibrium modules?: similarities, differences, and their likely causes, Atmos. Environ., 34, 117–137, 2000.

ACPD
14, 541–591, 2014

Table 1. Original size channels of OPC Grimm 1.107 calibrated with PLS (left side) and corrected (right side, columnar average) for the ambient refractive index determined over TR, MI and ME.

Intrument size OPC Channel	PLS (µm)	Ambient size (µm) Terni	Milano	Merano
1	0.25	0.27	0.27	0.26
2	0.28	0.30	0.30	0.30
3	0.30	0.32	0.33	0.32
4	0.35	0.38	0.39	0.38
5	0.40	0.46	0.47	0.45
6	0.45	0.52	0.53	0.52
7	0.50	0.56	0.58	0.56
8	0.58	0.75	0.79	0.75
9	0.65	0.80	0.91	0.81
10	0.70	0.90	0.94	0.90
11	0.80	1.00	1.06	1.00
12	1.00	1.35	1.35	1.33
13	1.30	1.78	1.78	1.78
14	1.60	2.14	2.14	2.14
15	2.00	2.40	2.40	2.40
16	2.50	2.82	2.82	2.82
17	3.00	3.67	3.67	3.67
18	3.50	4.62	4.62	4.62
19	4.00	5.01	5.01	5.01
20	5.00	5.89	5.89	5.89
21	6.50	9.55	9.55	9.55
22	7.50	10.72	10.72	10.72
23	8.50	12.16	12.16	12.16
24	10.00	16.03	16.03	16.03
25	12.50	22.65	22.65	22.65
26	15.00	29.85	29.85	29.85
27	17.50	37.15	37.15	37.15
28	> 20.00	> 44.67	> 44.67	> 44.67

ACPD
14, 541–591, 2014

Table 2. Comparison of the columnar optical and size distribution properties of the aerosol derived over MI from vertical profile measurements and over AERONET-Ispra site (~ 57 km from MI). n and k are the real and immaginary part of the complex refractive index. SSA is the Single Scattering Albedo. AOD and AOD_Abs are the Aerosol Optica Depth and the Absorption Aerosol Optical Depth, respectively. D_g and σ_g are the geometric mean diameter and the geometric standard deviation, respectively.

Parameter	Atmospheric Column AERONET – Ispra (235 m)			PROFILES – Milano (136 m)		
	441 nm	675 nm	870 nm	441 nm	675 nm	880 nm
n	1.415(±0.047)	1.418(±0.046)	1.425(±0.044)	1.500(±0.003)	1.500(±0.004)	1.494(±0.004)
k	0.032(±0.009)	0.029(±0.006)	0.030(±0.007)	0.032(±0.003)	0.030(±0.003)	0.030(±0.003)
SSA	0.812(±0.028)	0.778(±0.028)	0.740(±0.034)	0.857(±0.013)	0.846(±0.011)	0.812(±0.012)
AOD	0.232(±0.091)	0.124(±0.052)	0.083(±0.035)	0.274	0.152	0.092
AOD_Abs	0.050(±0.023)	0.032(±0.015)	0.025(±0.012)	0.047	0.028	0.020
D_g (µm)	0.206(±0.016)	0.206(±0.016)	0.206(±0.016)	0.204(±0.010)	0.204(±0.010)	0.204(±0.010)
σ_g	1.552(±0.045)	1.552(±0.045)	1.552(±0.045)	1.560(±0.060)	1.560(±0.060)	1.560(±0.060)

ACPD
14, 541–591, 2014

Table 3. Comparison of the Free Troposphere optical and size distribution properties of the aerosol derived from OPAC continental average data and over AERONET-Davos site. n and k are the real and immaginary part of the complex refractive index. SSA is the Single Scattering Albedo. AOD and AOD_Abs are the Aerosol Optica Depth and the Absorption Aerosol Optical Depth, respectively. D_g and σ_g are the geometric mean diameter and the geometric standard deviation, respectively.

Parameter	Free Troposphere AERONET – Davos (1596 m)			PROFILES – FT (> 1000 m)		
	438 nm	676 nm	870 nm	441 nm	675 nm	880 nm
n	1.449(±0.009)	1.468(±0.010)	1.482(±0.010)	1.511(±0.006)	1.510(±0.006)	1.501(±0.006)
k	0.010(±0.004)	0.010(±0.005)	0.011(±0.005)	0.011(±0.001)	0.011(±0.001)	0.011(±0.001)
SSA	0.950(±0.018)	0.947(±0.020)	0.941(±0.023)	0.955(±0.002)	0.932(±0.003)	0.897(±0.004)
AOD	0.036(±0.004)	0.022(±0.002)	0.015(±0.001)	0.039	0.014	0.006
AOD_Abs	$0.002(\pm 5 \times 10^{-4})$	$0.001(\pm 4 \times 10^{-4})$	$0.001(\pm 3 \times 10^{-4})$	0.002	0.001	0.001
D_g (µm)	0.269(±0.011)	0.269(±0.011)	0.269(±0.011)	0.299(±0.001)	0.299(±0.001)	0.299(±0.001)
σ_g	1.637(±0.024)	1.637(±0.024)	1.637(±0.024)	1.111(±0.001)	1.111(±0.001)	1.111(±0.001)

ACPD
14, 541–591, 2014

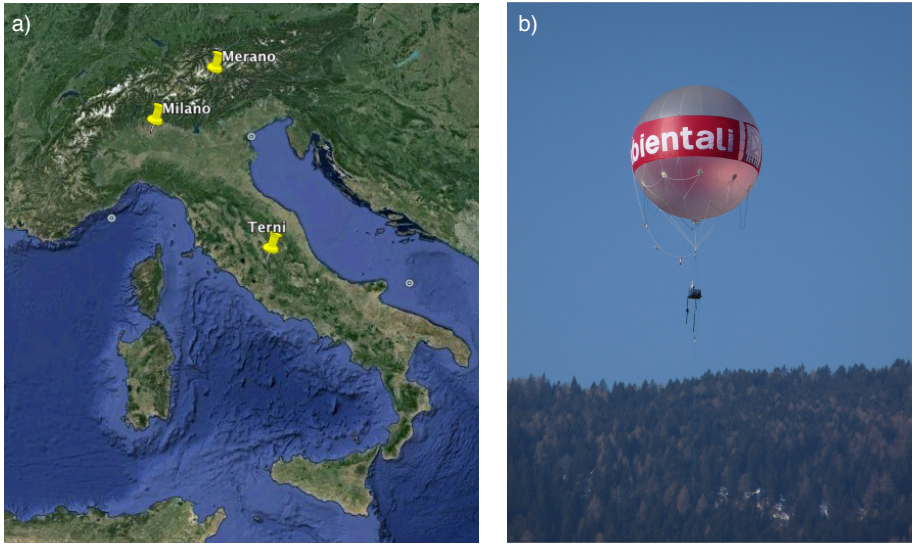

Fig. 1. (a) Location of the three sampling site: Terni in Central Italy (Terni Valley), Milano in Northern Italy (Po Valley) and Merano in the Alpine region (between of Passiria and Val Venosta Valleys); **(b)** tethered balloon flying over Merano with the instrumentation package.

ACPD
14, 541–591, 2014

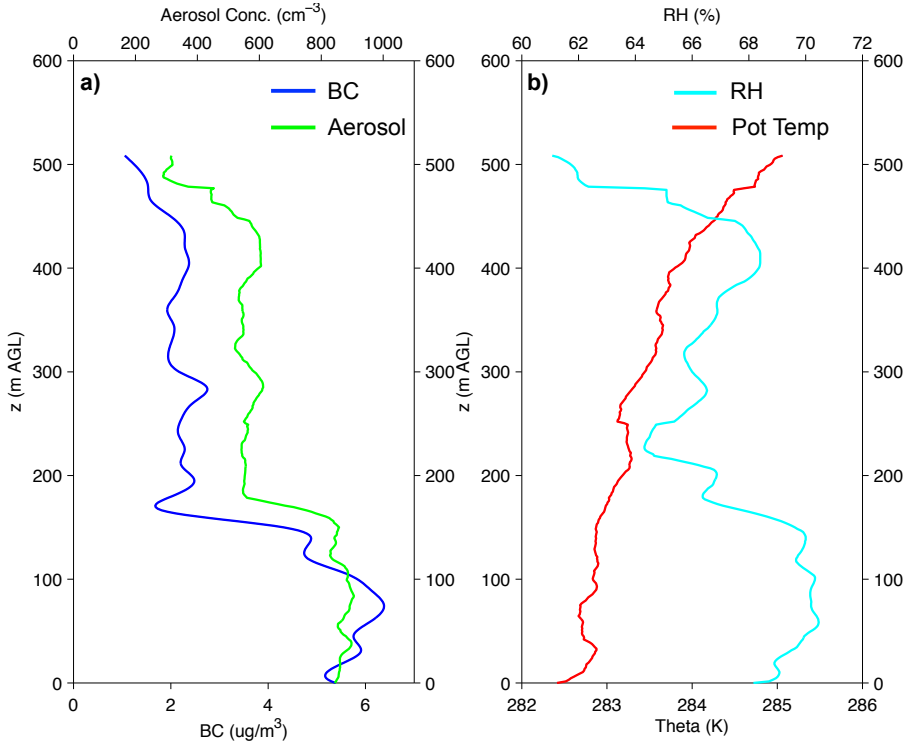

Fig. 2. Vertical profiles measured over TR on 28 January 2010 (13:45–14:26 UTC): **(a)** BC (blue line) and aerosol (green line, total particle number concentration cm^{-3}); **(b)** potential temperature (red line) and relative humidity (light blue line).

ACPD
14, 541–591, 2014

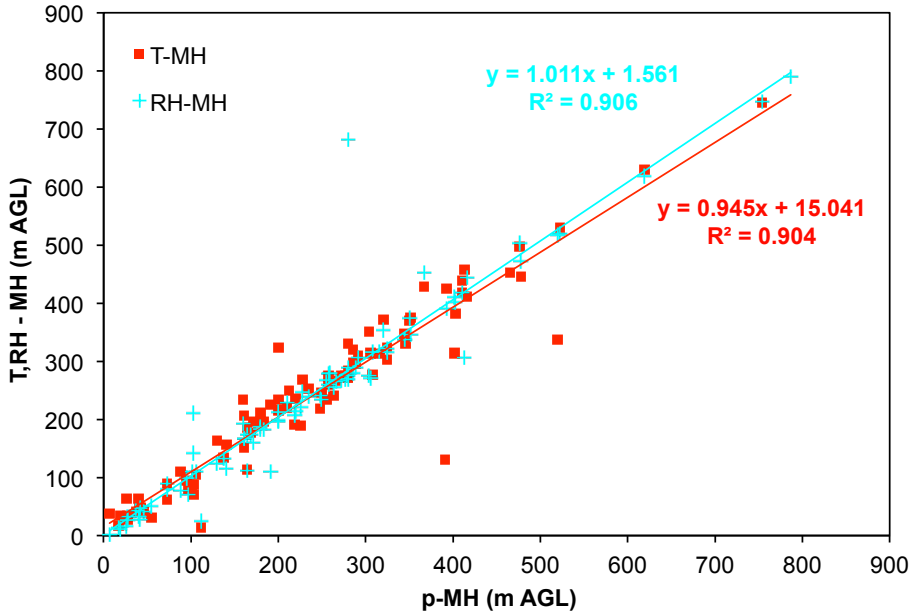

Fig. 3. Linear correlation between the mixing height derived from particle (p-MH) temperature (T-MH) and relative humidity (RH-MH) profiles

ACPD
14, 541–591, 2014

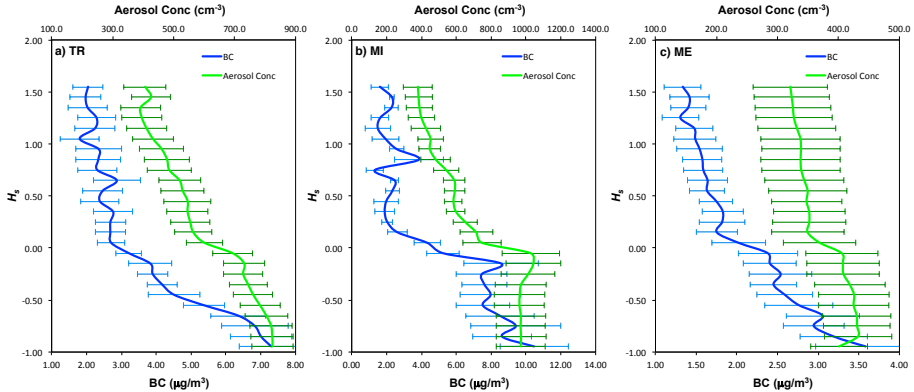

Fig. 4. The statistical mean profile of BC and aerosol concentrations along standardized height H_s for Terni **(a)**, Milan **(b)** and Merano **(c)**.

ACPD
14, 541–591, 2014

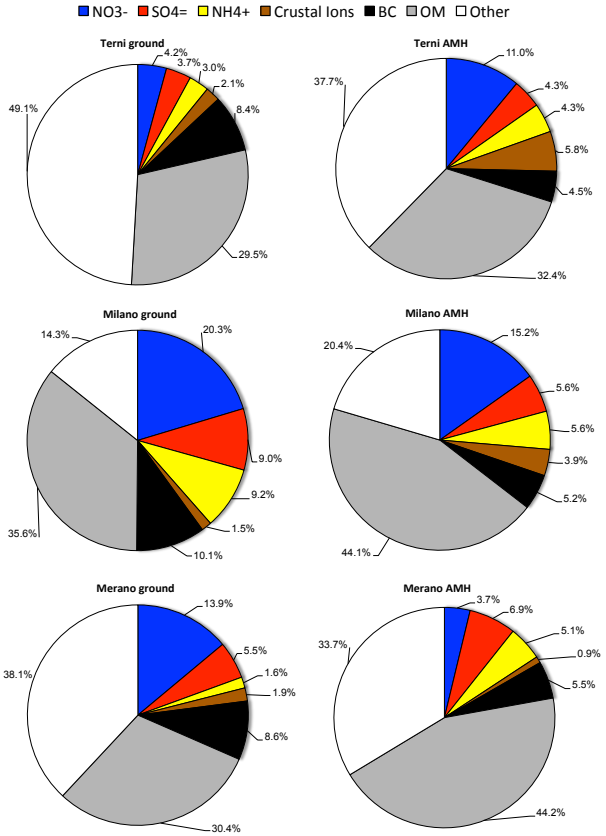

Fig. 5. Aerosol chemical composition, determined BMH and AMH for TR, MI and ME. Data shown are the respective aerosol mass fractions of each individual aerosol species.

ACPD
14, 541–591, 2014

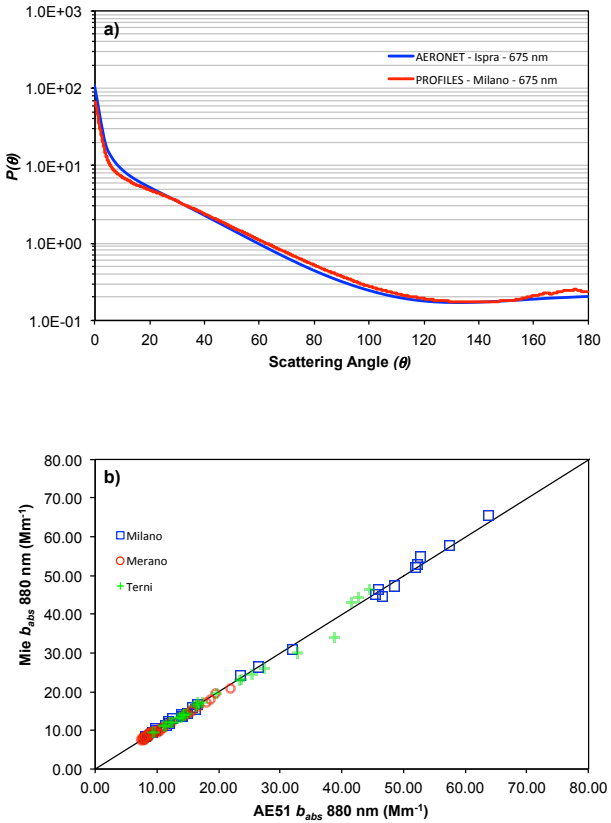

Fig. 6. (a) Aerosol Phase Function along the atmospheric column over MI and the one obtained at AERONET-Ispra; **(b)** linear correlation between the b_{abs} determined from Mie calculations and the one measured by the AE51 along vertical profiles for TR, MI and ME (the 1 : 1 black line is also plotted).

ACPD
14, 541–591, 2014

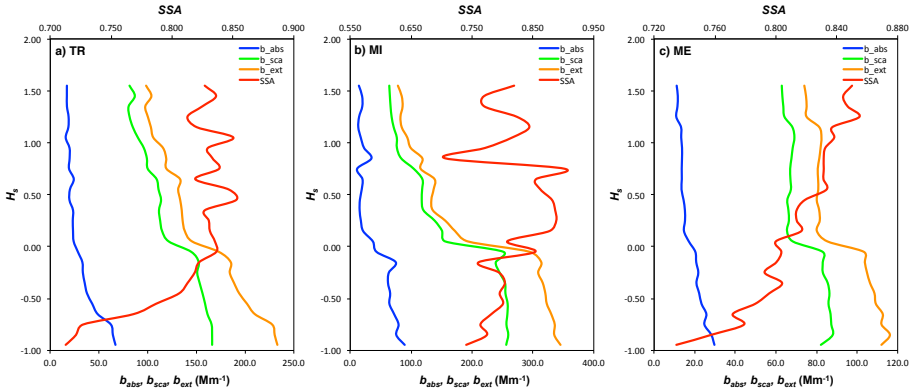

Fig. 7. Vertical profiles of aerosol optical properties (b_{abs}, b_{sca}, b_{ext}, SSA) at 675 nm over: **(a)** TR, **(b)** MI and **(c)** ME.

ACPD
14, 541–591, 2014

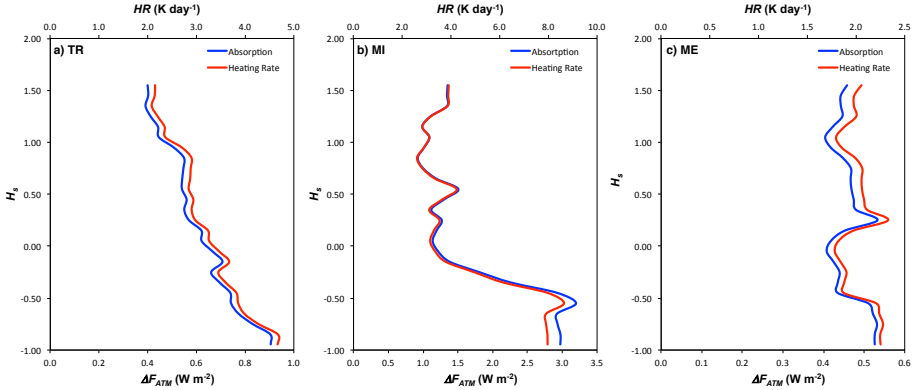

Fig. 8. BC-DRE and heating rates along vertical profiles over: **(a)** TR, **(b)** MI and **(c)** ME.

ACPD
14, 541–591, 2014